Noise amplification in open Taylor-Couette flow

Kenneth L. Babcock,* Guenter Ahlers, and David S. Cannell
Department of Physics and Center for Nonlinear Science, University of California, Santa Barbara, California 93106
(Received 22 February 1994; revised manuscript received 5 May 1994)

We present an extensive experimental and theoretical study of the flow in an open Taylor-Couette apparatus with radius ratio $r_1/r_2=0.738$ and imposed axial through-flow. Emphasis is given to the amplification of noise observed when the base flow is convectively unstable. Parameter boundaries for absolute and convective instability with respect to axisymmetric disturbances are determined experimentally and theoretically for axial Reynolds numbers $R \lesssim 4$, with excellent agreement between experiment and theory. Above onset a sustained pattern of traveling Taylor vortices is observed downstream of the inlet. In the case of absolute instability, the pattern is periodic within experimental resolution as evidenced by a narrow frequency spectrum in the time series of the Taylor-vortex velocity at a fixed point. In contrast, the patterns in the convectively unstable case arise *via* spatial amplification of microscopic noise. There results a broadened frequency spectrum caused by the pattern phase executing a pseudorandom walk. Virtually all aspects of the observed behavior are captured *quantitatively* by numerically integrating a complex Ginzburg-Landau (CGL) equation with an additive, spatially distributed, stochastic term. Precise measurements of the spatial amplitude profiles were made using fluids of various viscosities. The noise power required to fit the data has a viscosity dependence consistent with thermal noise, i.e., it has a "white" spectrum over at least a decade in frequency. Within our experimental uncertainty, the noise power is independent of the axial Reynolds number over the range $1.5 \lesssim R \lesssim 4$. Simulations of the stochastic CGL equation indicate that the noise corresponds to rms velocity fluctuations, which are smaller than typical fully developed secondary flows in our experiment by a factor of about 10^5. However, numerical evaluation of a recent theoretical result for the thermal noise power in the Taylor-Couette geometry with no through-flow turns out to be about 270 times smaller than the experimental result.

PACS number(s): 47.20.−k, 43.50.+y, 47.27.Sd

I. INTRODUCTION

"A deaf man might have seen the harmony." So remarked Leconte upon observing a torch flame dancing in synchrony to the strains of a cello [1]. This response to acoustic excitation is but one of many examples of the sensitivity of open flows to perturbations. It is well known that many open flows such as wakes [2], heated jets [3], free convection [4], and boundary layers [5–8] can respond to controlled, harmonic perturbations by amplifying a band of frequencies and wave numbers [9,10].

Amplification *via* instability renders open flows sensitive to noise as well as to periodic disturbances. This paper aims to demonstrate, by quantitative experimental and theoretical study, how macroscopic flow patterns can arise from amplification of intrinsic microscopic noise in a convectively unstable system [11,12]. Noise amplification is of great practical importance since all flows have unavoidable thermal or other noise sources. It is also central to the fundamental issue of stochastic effects in hydrodynamics [11,13], and in nonequilibrium spatially extended systems in general. This topic has stimulated a recent surge of attention, with little quantitative experimental work so far.

The system we studied was an open version of Taylor-Couette flow [14]. It consisted of fluid contained between two concentric cylinders with the inner one rotating and with through-flow imposed in the direction of the cylinders' axis. For a significant range of control parameters, rotating the inner cylinder causes the structureless base flow to become *convectively unstable,* i.e., individual perturbations of the base flow grow in a comoving frame but are advected downstream and out of the system [11,15,16]. No permanent secondary flow would exist in this regime in the absence of persistent perturbations or noise [12,17–19]. Yet one observes sustained, macroscopic patterns of traveling Taylor vortices downstream of the inlet [20–26]. We interpret these patterns as arising from the amplification of a persistent noise source by the convectively unstable system. The relevant noise is very small, having rms velocity fluctuations that are about 10^5 times smaller than typical velocities of the fully developed vortex pattern.

The work presented here focuses on small axial Reynolds numbers for which the primary instability is to traveling axisymmetric vortices. The topics we address are as follows.

Stability. The featureless base flow has parameter regimes of both convective and absolute instability. In the absolutely unstable case, disturbances grow in time at fixed positions and can fight their way upstream, nearly

*Present address: Digital Instruments, Inc., 520 E. Montecito St., Santa Barbara, CA 93103.

filling the entire system with a secondary vortex-flow structure that is periodic and insensitive to noise [15]. The simplicity of the Taylor-Couette geometry facilitates both a precise experimental measurement of the boundaries between the stability regimes, and a numerical calculation based on the Navier-Stokes equations. We find excellent agreement between experiment and theory [20,21].

Amplitude description. Virtually all observed properties of this system are captured *quantitatively* by a one-dimensional, complex Ginzburg-Landau (CGL) equation with a spatially distributed additive stochastic term and coefficients derived from the Navier-Stokes equations. This CGL equation should be applicable close to threshold. It affords a clear exposition of stability and the amplification mechanism, and provides for useful and efficient numerical simulation.

Characterization of noise-sustained structure. The convectively unstable system amplifies microscopic noise and leads to traveling vortex patterns [12,20,21,24–26]. Within the context of a stochastic Ginzburg-Landau equation, early emphasis has been given to these "noise-sustained structures" by Deissler [12]. The vortex amplitude grows spatially from an extremely small value at the system inlet to a nonlinearly saturated state sufficiently far downstream. Time series of the axial velocity at axial positions where the amplitude has saturated are nearly periodic in time, but their power spectra have nonzero width. The width is caused primarily by phase wander as opposed to variation in the flow amplitude. The difference between the measured phase and a perfectly periodic signal at the mean frequency executes a pseudorandom walk, i.e., the root-mean-squared phase deviation increases as a power law in time, but with an exponent slightly greater than 1/2. Properties of the secondary flow, such as spectral bandwidth and the phase autocorrelation time, are captured quantitatively by the linearized stochastic CGL equation.

Noise properties. We obtain an estimate of the experimental noise strength by comparing measurements of spatial amplitude profiles with CGL equation simulations, for which the noise strength is the only free parameter. We also numerically evaluate a recent theoretical calculation by Swift, Babcock, and Hohenberg [27] for the Taylor-Couette geometry, and find that at Reynolds number $R=3.0$ the experimental noise power is approximately 270 times larger than the prediction for thermal noise. Using a wide range of viscosities, and hence time scales, shows that the noise power is proportional to ν^{-2} as predicted by theory, or, equivalently, that it has a white spectrum over at least a decade in frequency. We also find that the noise power is, within the resolution of our measurements, independent of R for $1.5 \leq R \leq 4$, and that it is an order of magnitude smaller in our experiment than the noise floor reported by Tsameret, Goldner, and Steinberg [26] for $R \leq 2$.

In sum, the simple Taylor-Couette geometry allows precision experimental measurements and a detailed understanding of how instability of the primary flow amplifies intrinsic noise and leads to secondary flow structures. Experimental results can then be compared quantitatively with theoretical treatments of stochastic effects drawn from first principles. Furthermore, the streamwise constant boundary conditions and centrifugal nature of the instability avoid many of the complications typically found in the shear instabilities of most open flows, such as conditions that vary streamwise, secondary instabilities, and ill-defined boundary conditions.

This work can also be viewed as part of a larger effort to understand stochastic effects on pattern formation in nonequilibrium, spatially extended systems. For example, convective instability and noise amplification occurs also in closed systems with a Hopf bifurcation to traveling waves [28] and has been studied experimentally in binary-mixture convection [29]. In closed systems near bifurcations to a time-independent pattern, where the susceptibility of the pattern order parameter can become extremely large, noise-induced fluctuations can also become observable. This effect has been studied experimentally in electroconvection in nematic liquid crystals [30] and in gases at elevated pressures [31] where, just below the convection threshold, fluctuating patches of convection rolls arise in response to noise. An analogy can be drawn with order parameter fluctuations near equilibrium phase transitions. Noise amplification in open flows is perhaps more dramatic in that it leads to fully developed secondary flows, and occurs not just near bifurcation points but over the entire range of external conditions which render a system convectively unstable.

The paper is organized as follows. Section II describes the geometry and experimental setup. Section III gives an overview of the observed states and their stability vs control parameters. Section IV describes measurements of the onset of convective instability, and the numerical stability analysis used to calculate this boundary. Section V introduces the complex Ginzburg-Landau equation which we use to model noise amplification, and discusses the significance of absolute instability. Section VI discusses the onset of absolute instability from experimental and theoretical standpoints. Section VII describes noise-sustained structure, and how the essential observed properties can be understood in terms of the CGL model. Section VIII presents profile measurements which probe the power and viscosity dependence of the noise. The noise level is estimated by adjusting the noise power in simulations of the CGL equation to match the data. These results are compared with recent theoretical work [27] on thermal noise in the Taylor-Couette geometry, with our previous, less accurate measurements [21], and with the work of others [26].

In the remainder of this paper, we use a tilde to denote dimensioned lengths, times, and velocities in cases where confusion might arise. For the corresponding scaled variables the tilde has been dropped. The only exception is the parameter $\tilde{\epsilon}$, the dimensionless distance from the convective instability boundary.

II. EXPERIMENT

Our experiments used a concentric-cylinder Taylor-Couette apparatus with the inner cylinder rotating; the basic design is described in Ref. [32]. The outer cylinder

was machined from Lucite with an inner diameter $2\tilde{r}_2 = 5.160$ cm, 2.29 cm thick walls, and a total length of 1 m. The inner cylinder was machined from aluminum and finished with a Magnaplate [33] "HCR" hardcoating to resist nicks and prevent leaching of ions that promote unwanted flocculating of seed particles. The inner-cylinder diameter was $2\tilde{r}_1 = 3.806$ cm, giving a radius ratio $\eta \equiv \tilde{r}_1/\tilde{r}_2 = 0.738$ and a gap $d = \tilde{r}_2 - \tilde{r}_1 = 0.677 \pm 0.002$ cm. The total length of the working volume was $\tilde{L} = 97.5$ cm, yielding an aspect ratio $L \equiv \tilde{L}/d = 144$. We will scale lengths by d and time by the momentum diffusion time $\tau_d \equiv d^2/\nu$, where ν is the kinematic viscosity.

Hardened stainless steel shafts were attached to the inner cylinder and aligned, and the cylinder ends were finished with Delrin caps to prevent galvanic corrosion and to provide a smooth, azimuthally uniform surface that minimized disturbance of the incoming flow. As shown in Fig. 1, Delrin endcaps were attached to the outer cylinder, and held stainless steel ball bearings that supported the inner cylinder. The working fluid was contained by radial shaft seals made of a proprietary high molecular weight material [34] that minimized shaft wear. The cylinders were mounted horizontally, and were concentric and straight to ± 0.004 cm.

Through-flow was generated by a recirculating gravity feed with a fixed pressure head. The volume flow rate Q was controlled by an adjustable clamp applied to flexible tubing and was measured by a Manostat 36-547 TF flowmeter. The axial Reynolds number was defined as

$$R \equiv \langle \tilde{w} \rangle d/\nu \ , \tag{2.1}$$

where $\langle \tilde{w} \rangle = Q/\pi(\tilde{r}_2^2 - \tilde{r}_1^2)$ is the mean axial flow velocity. It was determined with an accuracy of 0.1–0.5 % and remained constant over several hours.

For the experiments described here, it is critical that the flow be introduced to the working volume with minimal velocity disturbance and a high degree of azimuthal symmetry. Figure 1 shows a scale drawing of the fluid inlet region in the endcap which was used to distribute the flow. The fluid first entered an annular channel, then passed through a machined Lucite annulus containing eight holes, each of diameter 1.09 mm, producing jets of uniform intensity. After passing through another ring of 24 holes of diameter 2.26 mm, the flow was deflected by a flange. It then passed through two layers of stainless steel mesh with grid spacing 0.44 mm (aperture size 0.24 mm) and entered the cylinder gap. Measurements of the axial velocity vs aximuthal angle at constant radius within $z = 3$ of the entry point showed that the flow was uniform to $\pm 1\%$. Some of the earlier experimental work [20] used a flow distributor with a single ring of holes.

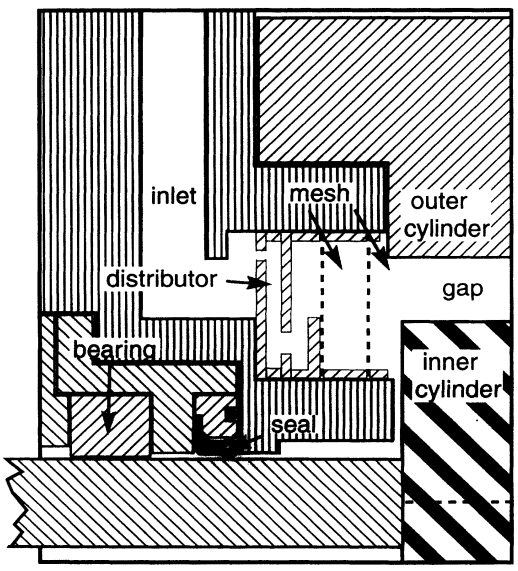

FIG. 1. Scale drawing of the inlet region of the apparatus.

Over the parameter range explored by us, the flow in the bulk of the apparatus was insensitive to the means by which it was extracted from the downstream end. In particular, it did not matter if the flow first passed through a layer of mesh, or simply passed through a hole at a single azimuthal position. The latter caused minor disturbances in the two or three vortices nearest the outlet, but did not affect the flow further upstream [25].

The working fluid consisted of water-glycerol mixtures ranging from pure water to 61% glycerol by volume, corresponding to a range of kinematic viscosities $0.935 < \nu < 10.0$ cS, and diffusion times $4.6 < \tau_d < 49.0$ s. The temperature of the fluid was maintained at 23.3 °C to a precision of 0.01 °C rms as it entered the apparatus. At the downstream end the temperature varied less than 0.04 °C, typically much less.

The inner cylinder was rotated by a stepper motor (Portescap model PH 632-508) driven by a microstepping driver (Parker Compumotor DB Drive). Depending on rotation frequency, we used between 400 and 5000 steps/revolution with step size chosen to optimize smoothness and frequency resolution. The latter was limited by the 1 μs resolution of a PC timer used to control the motor driver. Frequency resolution was always better than 0.1%, and could approach 0.01% as needed. High resolution was essential for determining parameters used in the noise estimates of later sections.

For flow visualization, the fluid was seeded with a Kalliroscope suspension [36]. We typically used 0.5–1.0 % by volume. Digitized images of the flow were captured by computer from a CCD camera. Seeding the fluid instead with 1.0 μm diameter polystyrene latex spheres with an approximate number concentration of $10^6/\text{cm}^3$ allowed point measurements of the axial flow velocity to a resolution of 0.005 cm/s using a home-built laser-Doppler velocimeter (LDV) [37] with a 1 s measuring time. The LDV was mounted on translation stages driven by stepper motors. To prevent flocculating of seed particles, the circulation loop included a cannister containing 2 cm^3 of 16–30 mesh beads of Dowex anionic and cationic resins (Dow-Corning No. 7780306).

The kinematic viscosity of the working fluid was measured using the known value of the Taylor number $\mathcal{T}$ at the primary onset to Taylor vortices with no through-flow. Linear stability analysis of the Navier-Stokes equations (Sec. IV) gave $\mathcal{T}_c = 2131.8$ for the critical Taylor number [38,39] for the radius ratio $\eta = 0.738$ assuming an

infinite geometry, where

$$\mathcal{T}=2\Omega_{\rm cyl}^2\eta^2 d^4/[\nu^2(1-\eta^2)]\ , \tag{2.2}$$

and $\Omega_{\rm cyl}$ is the angular frequency of the inner cylinder. Precise measurements of the onset frequency $\Omega_{{\rm cyl},c}$ were obtained by measuring the intensity of reflected light as a function of position. Alternatively, a very small through-flow was set up with negligible effect on onset ($R \ll 1$; see Sec. IV), and time series of axial velocity or reflected light were recorded as vortices slowly passed a fixed position. The resulting measurements were fitted to a harmonic function $a\cos(\Omega t+\phi_0)$ and the amplitude a extracted. The amplitude obeyed the expected relation $a^2 \propto \Omega_{\rm cyl}/\Omega_{{\rm cyl},c}-1$. Rounding at onset due to finite size effects [32,40] was minimal due to the large aspect ratio. The kinematic viscosity ν was then given *via* $\mathcal{T}_c$ with a typical overall precision of 0.02%.

III. OVERVIEW

This section gives a brief overview of stability and observed flow states that will be referred to in the rest of the paper.

Two control parameters describe the externally imposed conditions. One is the axial Reynolds number R given by Eq. (2.1). The second is the reduced angular rotation frequency of the inner cylinder

$$\epsilon\equiv\Omega_{\rm cyl}/\Omega_{{\rm cyl},c}(0)-1\ , \tag{3.1}$$

where $\Omega_{{\rm cyl},c}(0)$ refers to the onset of Taylor-vortex flow at $R=0$.

Except for a short inlet region to be discussed later, the featureless base flow is a superposition of azimuthal Couette flow $\tilde{V}_0(r)\hat{\theta}$ and axial Poiseuille flow $\tilde{W}_0(r)\hat{z}$, where we use right-handed cylindrical coordinates (r,θ,z). For a given Reynolds number R, this flow state is observed for sufficiently small ϵ. Discussions of stability refer to this base flow.

Figure 2 shows the parameter regime on which this paper is focused. There are two principal stability boundaries which we describe briefly; details of their measurement and calculation are given later.

The lower solid curve and data points locate the onset of *convective* instability, denoted $\epsilon_c(R)$. Below this boundary, the featureless base flow is stable. For $\epsilon>\epsilon_c(R)$, the base flow is unstable to the growth of traveling Taylor vortices. Perturbations can grow and spread, but are advected downstream and out of the system. An example from experiment is given in Fig. 3, which shows the development of an externally generated, macroscopic pulse of Taylor vortices. The boundary $\epsilon_c(R)$ curves up quadratically for small R, reflecting the well-known result that the axial flow suppresses the onset of vortex flow. This primary instability to traveling vortices was the subject of several early experimental and theoretical studies, although its convective nature was not emphasized [41]. More recent work has been directed toward exploring the rich variety of flow regimes, including traveling spirals and complex time-dependent states, that can be observed over a range of axial Reynolds numbers and rotation rates greater than those considered here [42–44].

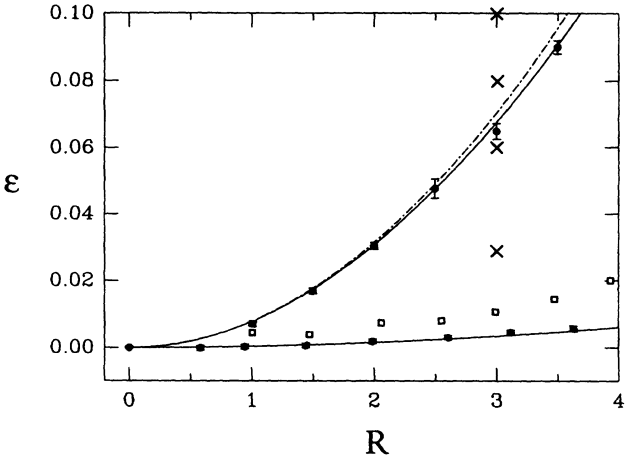

FIG. 2. Stability diagram for axisymmetric traveling vortices. The lower solid points and solid curve are the experimental and theoretical results, respectively, for the onset of convective instability at $\epsilon_c(R)$. The upper solid data points mark the experimental boundary between a broadened and a sharp frequency spectrum, and the upper solid curve is the theoretical result for the absolute instability boundary $\epsilon_a(R)$. The dash-dotted curve is the absolute instability boundary of the Ginzburg-Landau equation. The open squares are the minimum ϵ at which noise-sustained traveling vortices were observed with flow visualization at $z=100$. The crosses mark parameter values for the space-time plots of Fig. 4 below.

The upper solid curve in Fig. 2 is the result of the numerical evaluation of the onset of *absolute* instability $\epsilon_a(R)$ based on the full Navier-Stokes equations. Above it, disturbances of the base flow grow in a fixed frame, i.e., they can fight their way upstream. After transients die away, the system becomes nearly filled with a travel-

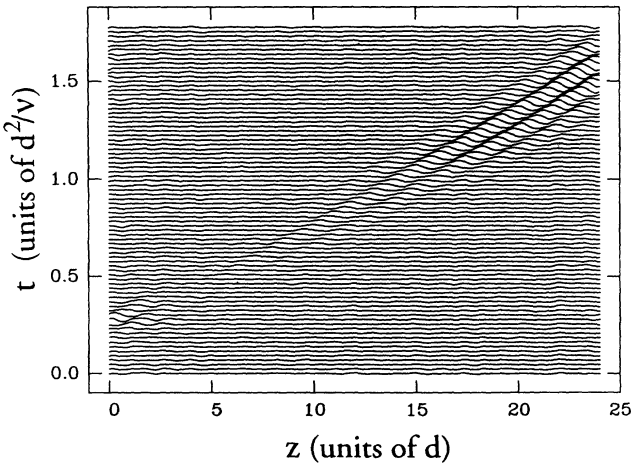

FIG. 3. Growth of a pulse of Taylor vortices in the convectively unstable regime; $R=16.5$ and $\epsilon=0.160$. At time $t=0.2$, the apparatus was rocked back and forth once about its axis. The length shown is about $L/6$.

ing vortex pattern, except near the inlet where the vortex amplitude must grow from zero, or near zero, because the flow enters with no rotation. The nearby data points mark the experimental minimum ϵ for which the traveling vortex pattern is periodic; for smaller ϵ, the spectrum becomes broadened. We show below that this transition corresponds to the boundary $\epsilon_a(R)$ between the convective and absolute instability regimes. The dot-dashed line is the transition from convective to absolute instability in the Ginzburg-Landau description presented in Sec. V.

Figure 4 shows space-time plots obtained by flow visualization of the observed *steady-state* flow at various ϵ for fixed $R=3.0$. In all cases, no external perturbations were applied, and transients were allowed to die down. In (a) and (b), the baseflow is absolutely unstable. A fully developed pattern of traveling vortices that grows spatially from zero at $z=0$ has been established in each case. A characteristic length, or *healing length* l_h of this growth, can be defined as the distance from $z=0$ required for the pattern to reach half of its saturated amplitude. The healing length increases as ϵ decreases, as can be seen in Fig. 4.

In Figs. 4(c) and 4(d), the base flow is convectively unstable. Sustained patterns of travelling vortices persist in this regime despite the fact that no external perturbations are applied. Numerical studies of thermal convection with through-flow have found that, in the absence of noise, patterns resembling those in Fig. 4 arose only in the absolutely unstable regime [17–19]. As ϵ was reduced, the characteristic length l_h diverged at the boundary ϵ_a between convective and absolute instability, and no patterns whatsoever were observed for $\epsilon<\epsilon_a$. We will show that the patterns of Figs. 4(c) and 4(d) arise from the amplification of microscopic noise. Such *noise-sustained patterns* are in fact observed throughout most of the convectively unstable regime $\epsilon_c<\epsilon<\epsilon_a$. The square data points of Fig. 2 show the minimum ϵ at which macroscopic vortex patterns were observed with flow visualization at $z=100$. As will be shown in Sec. VIII D these smallest detectable flow amplitudes correspond to vortices with an axial velocity amplitude of about 13 μm/s superimposed on the axial base flow.

The parameter space we consider is for the most part restricted to $R\lesssim 4.0$ because, at larger R, spirals are observed within the convectively unstable region, and they compete with the axisymmetric modes [20,44–46].

We now turn to a detailed discussion of stability.

IV. CONVECTIVE INSTABILITY

A. Measurement of onset

To determine the onset of convective instability we used artificially produced pulses of traveling vortices similar to that shown in Fig. 3. The pulses were produced by rotating both cylinders back and forth once

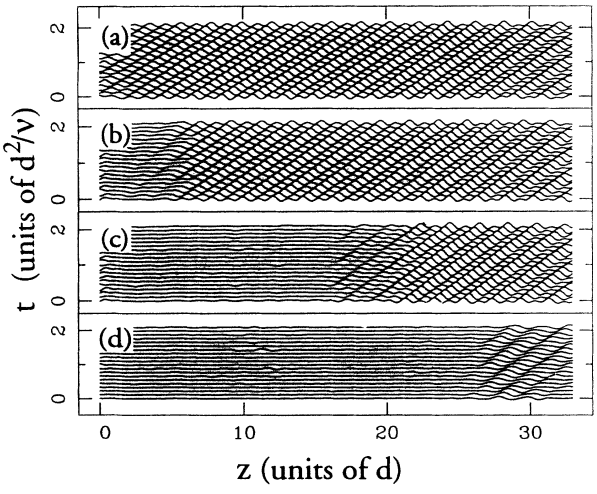

FIG. 4. Space-time plots of traveling vortex patterns, with no external perturbations, for the parameter values shown as crosses in Fig. 2. The Reynolds number was $R=3.0$, the viscosity was $\nu=0.025$ S, and ϵ was (a) 0.10, (b) 0.08, (c) 0.06, and (d) 0.035. The base flow was absolutely unstable for (a) and (b) and convectively unstable for (c) and (d). Note the increase of the healing length l_h as ϵ decreases. About $\frac{1}{4}$ of the apparatus is shown.

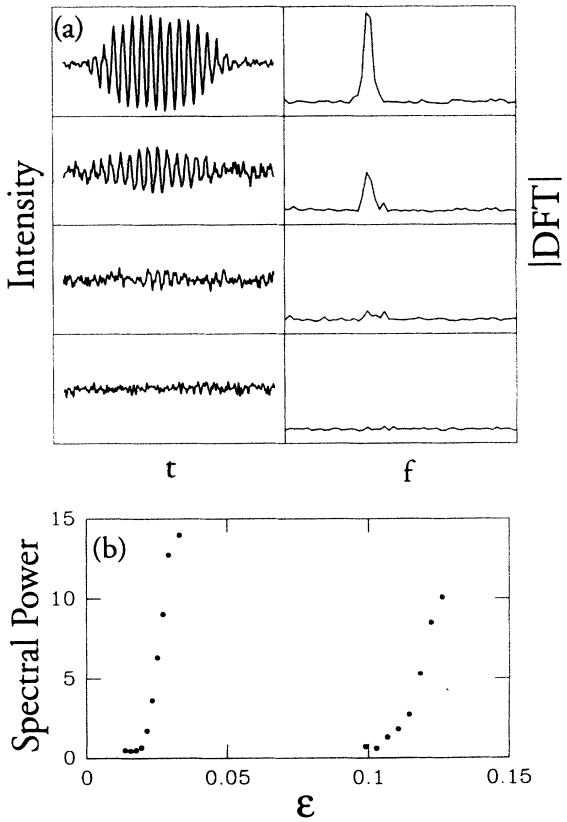

FIG. 5. (a) Time series of reflected light as vortex pulses passed a fixed axial position $z=100$, and corresponding discrete Fourier transform moduli, for $R=6.8$. Top to bottom: $\epsilon-\epsilon_c=0.0087$, 0.0048, 0.0009, −0.0030. (b) DFT peak power vs ϵ for $R=6.8$ (left) and 13.2 (right).

through a small angle about their axes. Reproducible, macroscopic disturbances were created by mounting the apparatus on bearings, and rotating with a stepper motor linked by a belt to an endcap. Typical rotations were 1° during 0.1 s, with a pause of 1–2 s before reversing direction; the resulting disturbances were considerably smaller than the one in Fig. 3. Fluid dragged azimuthally by the stainless steel mesh in the upstream endcap gave a localized disturbance with broad frequency and wave number content overlapping the band of amplified modes [47]. The result in the case of convective instability is shown in the space-time plot of Fig. 3. A visible pulse of two or three vortex pairs appeared at the inlet and traveled downstream. The pulse initially decayed over a fraction of the distance $\langle \tilde{w} \rangle \tau_d$, which is approximately that required for the inlet flow to attain the angular momentum of the base flow. The pulse then spread, grew in amplitude, and was advected out of the system.

Onset was measured by recording time series of light reflected from the Kalliroscope as pulses passed a point $z=100$ from the inlet; see Fig. 5(a). The amplitude of the fundamental peak in the discrete Fourier transform (DFT) was found for pulses at various ϵ for given R. Reducing ϵ caused slower pulse growth, and hence weaker signals at the observation point. As shown in Fig. 5(b), the intersection of the DFT peak amplitude with the noise baseline was taken as the onset [48] of convective instability ϵ_c. The data points in Fig. 6 show the results for $R \lesssim 20$. At larger R, spiral modes [46] grew and complicated the measurements [20]. These observations agree with recent calculations by Deissler [45] which predict spirals at onset for $R \gtrsim 18$ in our geometry.

B. Numerical stability analysis

We performed a numerical stability analysis of the base flow for our radius ratio to determine $\epsilon_c(R)$ for comparison with experiment. Similar calculations for different radius ratios have been done previously [41,46]; we present an outline of the calculations for completeness.

Using right-handed cylindrical coordinates $(\tilde{r},\tilde{\theta},\tilde{z})$, the (dimensioned) base flow in the idealized infinite system is $\tilde{V}_0(\tilde{r})\hat{\theta}+\tilde{W}_0(\tilde{r})\hat{z}$ where

$$\tilde{V}_0(\tilde{r})=\Omega_{\rm cyl}(\tilde{r}_1^2/\tilde{r}-\eta^2\tilde{r})/(1-\eta^2) \tag{4.1a}$$

and

$$\tilde{W}_0(\tilde{r})=2\langle \tilde{w} \rangle \frac{[1-(\tilde{r}/\tilde{r}_2)^2-(1-\eta^2)\ln(\tilde{r}/\tilde{r}_2)/\ln(\eta)]}{[1+\eta^2+(1-\eta^2)/\ln(\eta)]} . \tag{4.1b}$$

We let (u,v,w) be the dimensionless velocity deviation around this base flow. Scaling length by the gap d, time by d^2/ν, pressure p by $p\Omega_{\rm cyl}\nu/d$, and *in this section only* velocity [49] by $\Omega_{\rm cyl}\tilde{r}_1$, the Navier-Stokes equations linearized around Eq. (4.1) appear in cylindrical coordinates as

$$\frac{\partial u}{\partial t}+R^\theta\left[\frac{V_0}{r}\frac{\partial u}{\partial\theta}-\frac{2uV_0}{r}\right]+RW_0\frac{\partial u}{\partial z} = -\frac{\partial p}{\partial r}+\left[\nabla^2-\frac{1}{r^2}\right]u-\frac{2}{r^2}\frac{\partial v}{\partial\theta} ,$$

$$\frac{\partial v}{\partial t}+R^\theta\left[\frac{V_0}{r}\frac{\partial v}{\partial\theta}+u\frac{\partial V_0}{\partial r}+\frac{uV_0}{r}\right]+RW_0\frac{\partial v}{\partial z} = -\frac{1}{r}\frac{\partial p}{\partial\theta}+\left[\nabla^2-\frac{1}{r^2}\right]v+\frac{2}{r^2}\frac{\partial u}{\partial\theta} , \tag{4.2a}$$

$$\frac{\partial w}{\partial t}+R^\theta\frac{V_0}{r}\frac{\partial w}{\partial\theta}+R\left[W_0\frac{\partial w}{\partial z}+u\frac{\partial W_0}{\partial r}\right]=-\frac{\partial p}{\partial z}+\nabla^2 w ,$$

and continuity is

$$\frac{1}{r}\frac{\partial}{\partial r}(ru)+\frac{1}{r}\frac{\partial v}{\partial\theta}+\frac{\partial w}{\partial z}=0 . \tag{4.2b}$$

In Eqs. (4.2), $V_0=\tilde{V}_0/\Omega_{\rm cyl}\tilde{r}_1$ and $W_0=\tilde{W}_0/\Omega_{\rm cyl}\tilde{r}_1$, and the azimuthal Reynolds number is

$$R^\theta\equiv\Omega_{\rm cyl}\tilde{r}_1 d/\nu=\{\mathcal{T}(1+\eta)/[2(1-\eta)]\}^{1/2} .$$

Equations (4.2) admit traveling-mode solutions

$$(u,v,w,p)=[u(r),v(r),w(r),p(r)]e^{i(m\theta+kz-\Omega t)} , \tag{4.3}$$

where k and Ω are in general complex, and m is real and describes the azimuthal pitch. We will focus on axisymmetric structures ($m=0$). Stability analysis for spiral modes ($m\neq 0$) has been done elsewhere [45,46].

Inserting (4.3) into (4.2) gives a series of ordinary differential equations for the complex radial functions (u,v,w,p). These can be recast as a first order system for $\vec{U}=(u,v,w,p,dv/dr,dw/dr)$

$$\frac{d\vec{U}}{dr}=\mathbf{A}\vec{U} \tag{4.4}$$

where $\mathbf{A}=[a_{ij}]$ is dependent on the parameters k, Ω, R, and R^θ

We solved Eq. (4.4) by a shooting method. Three independent solutions $\vec{U}^1(r)$, $\vec{U}^2(r)$, $\vec{U}^3(r)$ were generated

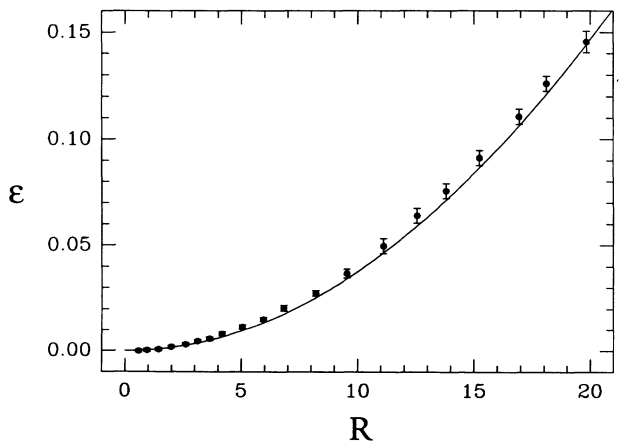

FIG. 6. Convective instability boundary $\epsilon_c(R)$. Data points were obtained by observing pulse growth. The curve is the linear stability result.

by numerically integrating Eq. (4.4) from $r=r_1$ to $r=r_1+1$ using initial values (0,0,0,1,0,0), (0,0,0,0,1,0) and (0,0,0,0,0,1). The solution $\vec{U}=C_1\vec{U}^1+C_2\vec{U}^2+C_3\vec{U}^3$ must satisfy no-slip boundary conditions $U_1=U_2=U_3=0$ (i.e., $u=v=w=0$) at $r=r_1$ and $r=r_1+1$. This gives three homogeneous equations for the C_i that define a complex eigenvalue problem which has a solution when

$$F(k,\Omega,R,R^\theta)=\begin{vmatrix} U_1^1 & U_1^2 & U_1^3 \\ U_2^1 & U_2^2 & U_2^3 \\ U_3^1 & U_3^2 & U_3^3 \end{vmatrix}=0 \tag{4.5}$$

at $r=r_1+1$ with k constrained to be real. For given axial Reynolds number R, the goal is to find R_c^θ, i.e., the minimum of R^θ with respect to k for which the growth rate $\Omega^i\equiv\mathrm{Im}(\Omega)=0$.

In practice the ordinary differential equations (ODE's) Eq. (4.4) are integrated using a fourth-order Runge-Kutta routine with at least 100 radial steps. For given R, a secant search determines the complex frequency $\Omega(k,R^\theta)$ that satisfies Eq. (4.5), with a zero constraint better than 10^{-7} on the determinant. For given R^θ, this is repeated for various k to find the value k_0 for which the growth rate Ω^i is a maximum. R^θ is then adjusted until $\Omega^i(k_0)=0$, giving the critical values R_c^θ, k_c, and $\Omega_c^r=\Omega^r(k_c)$. The whole procedure is done for a range of axial Reynolds numbers R. Initial guesses at critical values stem from the known values for $R=0$. Fits to the results gave

$$k_c=3.136+0.000\,104R^2(1-0.000\,14R^2)\ , \tag{4.6a}$$

$$\Omega_c=3.677R(1+0.000\,020R^2)\ , \tag{4.6b}$$

and

$$\epsilon_c\equiv R_c^\theta(R)/R_c^\theta(0)-1 =0.000\,381R^2(1-9.3\times10^{-5}R^2)\ . \tag{4.6c}$$

Equation (4.6c) is shown in Fig. 6 and as the lower solid curve in Fig. 2. The agreement between experiment and theory is excellent. Equations (4.6) also agree with independent calculations by Recktenwald and co-workers [50].

V. GINZBURG-LANDAU DESCRIPTION

We have found that virtually all observed phenomena in the open Taylor-Couette system are captured *quantitatively* by a stochastic, complex Ginzburg-Landau equation. We write the dimensionless axisymmetric vortex flow field as

$$\vec{V}(r,z,t)=A(z,t)\vec{U}(r)e^{i(k_c z-\Omega_c t)}+\mathrm{c.c.}\ , \tag{5.1}$$

where as before length and time are scaled by the gap d and the diffusion time d^2/ν respectively, but where velocity henceforth is scaled by ν/d. The complex radial eigenfunction at onset $\vec{U}(r)$ was obtained in the course of the linear stability analysis of Sec. IV. Here $\vec{U}$ is restricted to the velocity components (u,v,w). For each value of the axial Reynolds number R, an expansion around the onset of convective instability [51] gives the one-dimensional complex Ginzburg-Landau description of the amplitude of the traveling vortex pattern:

$$\tau_0(\dot{A}+sA')=\tilde{\epsilon}(1+ic_0)A+\xi_0^2(1+ic_1)A'' -g(1+ic_2)|A|^2A+f_A(z,t)\ , \tag{5.2}$$

where primes denote spatial derivatives $\partial/\partial z$. Equation (5.2) contains the absolute instability and spatial amplification of perturbations. Furthermore, we will show in Secs. VII and VIII that numerical integration of Eq. (5.2) with the additive stochastic term $f_A(z,t)$ provides a quantitative simulation of the physical system that yields information about the magnitude and spectral properties of the noise.

A. Coefficients

The control parameter

$$\tilde{\epsilon}\equiv\Omega_{\mathrm{cyl}}/\Omega_{\mathrm{cyl},c}(R)-1=[\epsilon-\epsilon_c(R)]/[1+\epsilon_c(R)]$$

measures the distance above the onset of convective instability (in contrast to other variables in this paper, the tilde in this case obviously does not indicate a dimensioned variable). Coefficients of the linear terms were obtained according to standard definitions [51] *via* the stability analysis described in Sec. IV B. These were found numerically for $\eta=0.738$ and then fitted to the lowest two orders in R having the proper symmetry. The results are

$$\tau_0=\frac{1}{R_c^\theta}\left(\frac{\partial\Omega^i}{\partial R^\theta}\right)^{-1} =0.0379-0.000\,024R^2(1-0.000\,46R^2)$$

for the time scale,

$$s=\frac{\partial\Omega^r}{\partial k}=1.230R(1+0.000\,004\,1R^2)$$

for the group velocity,

$$\xi_0^2=\frac{1}{2R_c^\theta}\left(\frac{\partial^2R^\theta}{\partial k^2}\right) =0.0725-0.000\,048R^2(1-0.000\,53R^2)$$

for the correlation-length amplitude,

$$c_0=-\tau_0R_c^\theta\left(\frac{\partial\Omega^r}{\partial R^\theta}\right)=0.007\,20R(1-0.000\,38R^2)$$

for the linear frequency shift, and

$$c_1=\frac{\tau_0}{2\xi_0^2}\left(\frac{\partial^2\Omega^r}{\partial k^2}\right)=0.0235R(1+0.000\,26R^2)$$

for the dispersion. All derivatives are taken around the critical values of Ω, k, and R^θ. Over the parameter range of Fig. 2, the imaginary parts c_i are small, indicating that dispersion and frequency shifting are not significant. These results also agree with independent calculations by Recktenwald and co-workers [50].

The amplitude scale is set by the nonlinear coefficient g and the normalization of the eigenfunction $\vec{U}$. We chose a normalization $\int_{r_1}^{r_2}\vec{U}(r)\cdot\vec{U}^*(r)r\,dr=1$, where $\vec{U}(r)$ is restricted to its first three (velocity) components. The value of g_0 (the nonlinear coefficient at $R=0$) was determined experimentally by establishing a traveling vortex state with a very small value of R and measuring the vortex contribution to the axial flow velocity. This contribution is described by the axial component of Eq. (5.1), which can also be written as $V_z=W(r)\cos(kz-\Omega t+\phi)$ for a uniform amplitude flow state. The measurements were made at a fixed value of z and as a function of time. (Alternatively, measurements of V_z with $R=0$ and as a function of axial position gave equivalent results.) The LDV was set to the radius r_m where the measured $W(r)$ had a maximum. Time series of the axial velocity for various ϵ were fit to a background term plus V_z, giving the amplitude $W(r_m)$ as a function of ϵ. For a spatially uniform pattern near onset with $k=k_c$, Eqs. (5.1) and (5.2) give

$$W(r_m)=2\sqrt{\epsilon/g_0}|w(r_m)|\ ,$$

where w is the axial component of the eigenfunction [Eq. (4.3)]. Numerically we find $|w(r_m)|=0.300$ with $r_m=r_1+0.256$. Fitting $W(r_m)$ to the form above then gave $g_0=(8.35\pm0.1)\times10^{-4}$. A recent theoretical calculation [50] found $g_0=8.40\times10^{-4}$ in this scaling, in excellent agreement with our experiment. Experimentally, we found only a small change ($<5\%$) in g for R up to 3.

For the imaginary nonlinear coefficient, which gives a nonlinear frequency shift, we used $c_2=0.0113R$ in our CGL equation simulations. This value was calculated by Müller, Lücke, and Kamps for convection with throughflow [17]. Our results did not depend on the particular value of c_2 so long as it was small [52].

B. Absolute instability

It is straightforward to calculate the boundary for absolute instability within the context of Eq. (5.2). As a first illustration, consider the evolution [12] of a Gaussian amplitude perturbation $\delta A_0(z)=ae^{-\alpha z^2}$. Under the linear parts of Eq. (5.2), its evolution is dominated by the exponential factor

$$\delta A(z,t)\propto\exp\left[\epsilon\frac{t}{\tau_0}(1+ic_0)-\frac{\tau_0(z-st)^2}{4t\xi_0^2(1+ic_1)}\right]\ . \tag{5.3}$$

In the limit of large time, the amplitude at a fixed value of z will grow when

$$\epsilon>\epsilon_a^{\rm CGL}=\frac{\tau_0^2s^2}{4\xi_0^2(1+c_1^2)}\ , \tag{5.4}$$

which is in fact the rigorous condition for absolute instability. The boundary $\epsilon_a^{\rm CGL}$ is plotted vs R as the dot-dashed line in the stability diagram Fig. 2. We may rewrite this condition as

$$s<2\frac{\xi_0}{\tau_0}\sqrt{\epsilon(1+c_1^2)}\ , \tag{5.5}$$

which says that the perturbation will grow at fixed z if it moves downstream more slowly than the rate at which it spreads in a frame moving at the group velocity. Equality in Eq. (5.5) would be the result for the velocity of a pattern front [53].

The condition for absolute instability can be examined in a more general way that extends usefully to numerical stability analysis [12,15,16]. An amplitude perturbation of arbitrary shape can be expanded in traveling modes according to

$$\delta A(z,t)=\int_{-\infty}^{\infty}\delta A(q)e^{i[qz/t-\omega(q)]t}dq\ , \tag{5.6}$$

where

$$q=k-k_c$$

and

$$\omega=\Omega-\Omega_c$$

are deviations from the critical wave number and frequency. Equation (5.2) gives the complex dispersion relation for linear perturbations

$$\omega(q)=qs+\frac{\epsilon}{\tau_0}(i-c_0)+\frac{\xi_0^2q^2}{\tau_0}(c_1-i)\ , \tag{5.7}$$

where ω and q are in general complex. Using the method of steepest descent, the long-time behavior of Eq. (5.6) along a ray described by fixed z/t is dominated by the saddle point q_s defined by

$$\begin{aligned}&{\rm Re}\left[\frac{d\omega}{dq}\right]\Big|_{q_s}=\frac{z}{t}\ ,\\ &{\rm Im}\left[\frac{d\omega}{dq}\right]\Big|_{q_s}=0\ .\end{aligned} \tag{5.8}$$

That is, in a frame moving at velocity z/t, the amplitude is eventually dominated by the least stable mode with a (real) group velocity equal to z/t, and the growth rate along this ray is ${\rm Re}[iq_sz/t-i\omega(q_s)]$. A wave packet that eventually grows in some frame is confined between two rays on which the growth rate is zero [16].

To examine absolute instability, we consider a fixed position z at large times ($z/t\to0$). Equation (5.8) shows that the amplitude is then governed by the mode with zero group velocity. Relative to k_c, Eqs. (5.7) and (5.8) give for the saddle point

$$\begin{aligned}q_s^i&=-\frac{s\tau_0}{2\xi_0^2(1+c_1^2)}\ ,\\ q_s^r&=c_1q_s^i\ .\end{aligned} \tag{5.9}$$

The growth rate $\omega^i(q_s)$ determines the nature of the instability. Setting $\omega^i(q_s)=0$ yields the onset for absolute instability ϵ_a as in Eq. (5.4). For absolute instability, $\omega^i(q_s)>0$, and a packet grows at a fixed point, whereas $\omega^i(q_s)<0$ corresponds to convective instability, so long as

there is some ray z/t along which the growth rate is positive [54].

The transition from convective to absolute instability thus involves the frame of reference, but no new instability mechanisms. Any sustained secondary flows in a convectively unstable flow must originate from a persistent source of continuous forcing or noise. However, as the above treatment indicates, any small forcing is relatively unimportant in the absolutely unstable case, because such a flow is dominated by the mode with positive growth rate $\omega^i(q_s)$.

C. Simulation with noise

To model stochastic effects, we use a complex additive noise term [13,21,55,56] $f_A(z,t)$ with the properties

$$\langle f_A(z,t)\rangle = \langle f_A(z,t) f_A(z',t')\rangle = \langle f_A^*(z,t) f_A^*(z',t')\rangle = 0 \ , \tag{5.10}$$

$$\langle f_A(z,t) f_A^*(z',t')\rangle = 2\xi_0\tau_0 F_A \delta(z-z')\delta(t-t') \ .$$

This form for the noise term gives fluctuations in the (linearized) amplitude response [57]

$$\langle |A|^2\rangle = F_A/2|\tilde{\epsilon}|^{1/2} \tag{5.11}$$

for $\tilde{\epsilon}<0$ and $R=0$. A discrete version of Eq. (5.2) was numerically integrated using a Crank-Nicholson implicit forward-differencing algorithm [58]. An aspect ratio of $L=120$ was used in most cases, with a maximum spatial step of $\Delta x=0.1$, and a maximum time step of $\Delta t=0.01$.

Noise was included by adding a random complex number $f=\gamma e^{i\phi}\sqrt{(\Delta t/\Delta x)}$ at each integration time step to the amplitude at each grid point, where γ is a real-valued Gaussian random variable [59] with variance $2\xi_0\tau_0 F_A$. The phase ϕ was random. We also tried a deterministic phase factor $\phi=-(k_c z-\Omega_c t)$, but in no instance did we find simulations of Eq. (5.2) to depend on this choice. The factor $\sqrt{\Delta t/\Delta x}$ gives proper scaling for uncorrelated noise, i.e., it ensures that $\langle |A|^2\rangle$ is independent of Δx and Δt.

At the upstream end we used the boundary condition (BC) $A(z=0)=0$. One might argue that the amplitude at the inlet should not be fixed, but rather that it should be allowed to fluctuate under the influence of the noise. However, this difference turned out to be unimportant for the downstream part of the system. To show this, we added a section between $z=-0.1$ and $z=0$ with $\tilde{\epsilon}=-0.1$. In the subcritical part, the fluctuating amplitude reached the rms value given by Eq. (5.11) and at $z=0$ the value of A thus fluctuated in a manner determined primarily by the noise level and by the subcritical value of $\tilde{\epsilon}$. A short distance into the main section $z>0$ with $\tilde{\epsilon}>0$, the rms value of the amplitude was nearly the same as before the addition of the subcritical section. At the downstream end, we tried various BC's. They had very little influence on the behavior in the system interior. For much of the work, we used vanishing-derivative BC's.

The stochastic CGL equation produces sustained patterns in the convectively unstable regime much like those shown in Figs. 4(c) and 4(d). Figure 7(a) shows a longer space-time plot of the sustained pattern observed in the experiment for $R=3.0$ and $\epsilon_c<\epsilon=0.044<\epsilon_a$. We mimicked the experiment by integrating Eq. (5.2) and plotting the "velocity function"

$$\Psi=\mathrm{Re}\{A(z,t)\exp[i(k_c z-\Omega_c t)]\}$$

at successive times for $R=3.0$,

$$\tilde{\epsilon}=0.040 \ (\epsilon=0.044) \ .$$

The result is shown in Fig. 7(b). The noise level was adjusted until the characteristic length l_h roughly matched that of the experiment, with the result $F_A\cong 2.1\times10^{-7}$. This is only a rough estimate of the noise level because the nonlinear response of the flow visualization makes the determination of l_h problematic; a more precise measurement of the amplitude profiles and of the noise level is discussed in Sec. VIII. As shown in Refs. [20] and [21] and discussed more fully in Sec. VIII D, the noise is microscopic in the sense that the corresponding rms velocity fluctuations are several hundred times smaller than can be measured using flow visualization techniques.

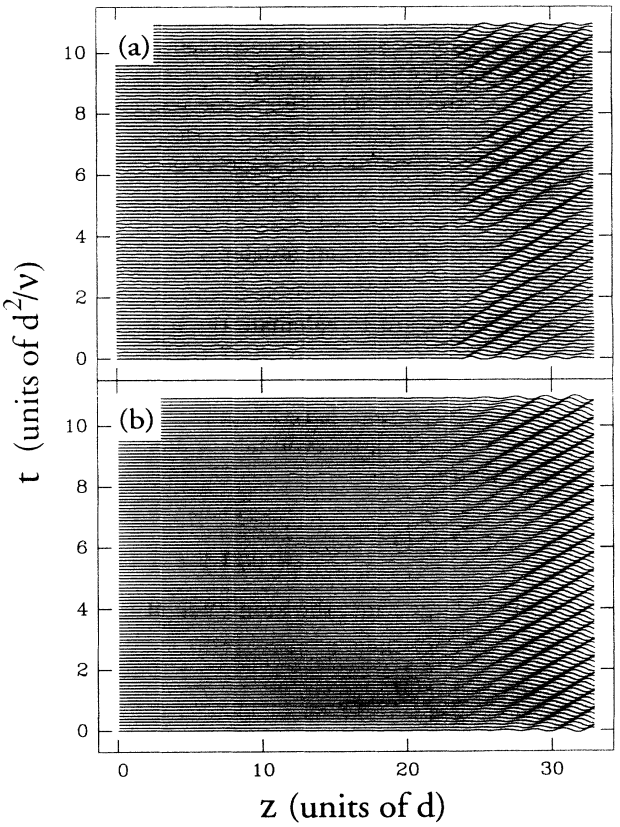

FIG. 7. Space-time plots of noise-sustained structure in the convectively unstable regime. (a) Experimental flow visualization with Kalliroscope for $R=3.0$, $\nu=0.025$ S, and $\tilde{\epsilon}=0.040$. (b) Integration of Eq. (5.2) with noise level $F_A=2.1\times10^{-7}$.

VI. ABSOLUTE INSTABILITY IN THE FULL SYSTEM

A. Navier-Stokes equations

In this section we calculate the onset of absolute instability in the full Eqs. (4.2). We employ a numerical procedure similar to that used in the calculation of the onset of convective instability in Sec. IV B, except that the wave number q is allowed to be complex. Again, for a given value of axial Reynolds number R, the onset of absolute instability occurs at the minimum value of R^θ for which the growth rate $\omega^i(q_s)=0$, where q_s is located at the saddle of the dispersion relation $\omega^i(q)$. The shooting method of Sec. IV B is used with the complex frequency ω adjusted to satisfy the zero determinant condition, Eq. (4.5). The growth rate ω^i is found over a grid of q^i and q^r. Quadratic fits of ω^i in the directions of q^i and q^r locate the saddle point q_s, and give the growth rate $\omega^i(q_s)$. This procedure is repeated to find the critical value of R^θ for which $\omega^i(q_s)=0$, and repeated overall for a range of axial Reynolds numbers R. Initial guesses for the critical azimuthal Reynolds number and the saddle point were taken from the Ginzburg-Landau expressions Eqs. (5.4) and (5.9).

Figure 8 shows the real and imaginary parts of the complex dispersion relation [the growth rate $\Omega^i(k)=\omega^i(k)$ and the frequency $\Omega^r(k)=\omega^r(k)+\Omega_c$] over a range of complex $k=k_c+q$ for convectively unstable

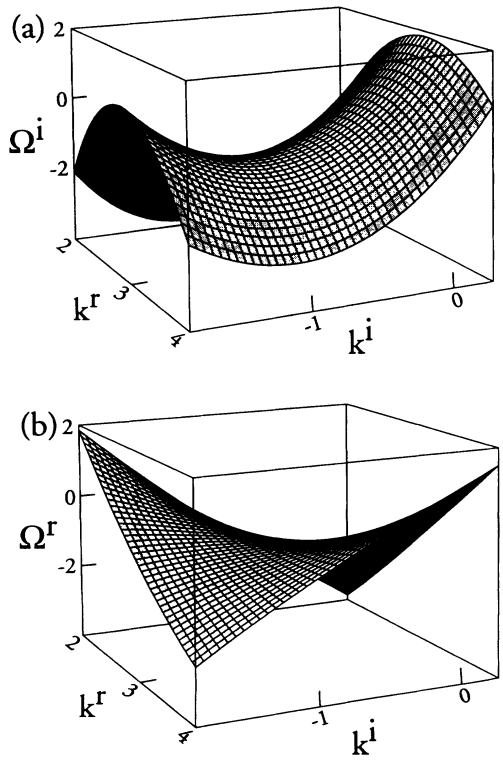

FIG. 8. Imaginary and real parts of the complex dispersion relation $\Omega(k)$ in the Navier-Stokes equations for convectively unstable conditions $\epsilon=0.036$ and $R=3.0$. (a) Growth rate Ω^i. (b) Angular frequency Ω^r.

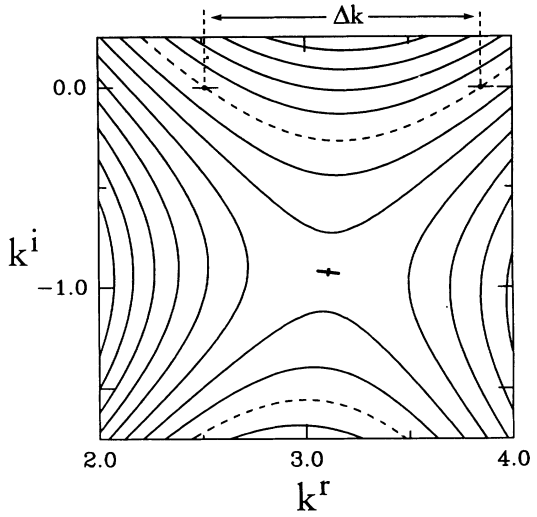

FIG. 9. Contour plot of growth rate Ω^i vs complex wave number for $\epsilon=0.036$ and $R=3.0$. Contour spacing is $\Delta\Omega^i=0.40$, and the dashed contours locate $\Omega^i=0$. The marker at the saddle point indicates the direction of steepest descent. Growth occurs for the band of real wave numbers Δk.

conditions $\epsilon_c<\epsilon=0.036<\epsilon_a$, at $R=3.0$. The saddle structure is clearly visible in Fig. 8(a). Figure 9 shows a contour plot for the growth rate Ω^i. The dashed curves correspond to $\Omega^i=0$. Their intersections with the real axis ($k^i=0$) shows that there is a band of real wave numbers for which perturbations grow, indicative of $\epsilon>\epsilon_c$. Since $\Omega^i<0$ at the saddle point, $\epsilon<\epsilon_a$. Increasing R^θ raises the dispersion surface with negligible change of shape.

The results for onset are well fitted by

$$\epsilon_a=0.007\,82R^2(1-0.0043R^2)\,, \tag{6.1}$$

shown as the upper solid curve in the stability diagram Fig. 2. This result is close to the Ginzburg-Landau expression obtained by putting the coefficient values of Sec. V A into Eq. (5.4), with the result

$$\epsilon_a^{\mathrm{CGL}}=0.007\,89R^2(1-0.0008R^2)\,. \tag{6.2}$$

Equation (6.1) is also in excellent agreement with the experimental result described in the next section. The close match of the CGL result Eq. (6.2) with the experiment and with the full equation result Eq. (6.1) suggests that the CGL Eq. (5.2) applies well throughout the parameter range of Fig. 2.

B. Experimental measurement

To locate ϵ_a, one might appeal to the definition of absolute instability and attempt to determine the ϵ for which a vortex front (separating the base flow at smaller z from vortex flow at larger z) moves neither upstream nor downstream. We tried this by launching vortex pulses such as that shown in Fig. 3, with the system initially convectively unstable ($\epsilon_c<\epsilon<\epsilon_a$). The pulses were al-

lowed to reach the middle region of the system, whereupon ϵ was suddenly increased into the absolutely unstable region. For large jumps in ϵ, pulses responded by beginning to spread upstream. We then attempted to locate the boundary ϵ_a by adjusting the jump in ϵ until the upstream edge was stationary after transients had died down. However, this method proved to be problematic. The time scale for the pulse boundaries to reach an asymptotic form is long enough that noise-sustained vortex structures such as those shown in Figs. 4(c) and 4(d) grew and engulfed the pulse, rendering the method useless.

We have found that sustained patterns such as those in Fig. 4 have characteristic signatures that serve as an alternative probe of the absolute instability boundary ϵ_a. For given ϵ and R, we recorded time series of light reflected from Kalliroscope as the vortices passed $z=100d$, far downstream of the inlet. As noted in Sec. III, the vortices persisted when ϵ was only slightly greater than ϵ_c. However, the frequency spectrum of the time series underwent a striking change when ϵ was increased sufficiently far above this boundary.

Figure 10 shows portions of time series, each covering about 160 periods, and corresponding discrete Fourier transform (DFT) moduli for various ϵ at $R=3.0$. In Fig. 10(a), $\epsilon=\epsilon_c+0.0896$, the data appear periodic and of nearly uniform amplitude, and the fundamental DFT peak is very sharp. In contrast, for $\epsilon=\epsilon_c+0.0318$ [Fig. 10(b)], the time series remains fairly uniform in amplitude, but the DFT peak has become broadened. Sustained patterns persist even for $\epsilon-\epsilon_c=0.0077$ [Fig. 10(c)], but the amplitude now shows time variation. This is because the characteristic length l_h has grown to near the measuring point $z=100$, and the amplitude in this region fluctuates.

A measure of the spectral width is the normalized second moment of the fundamental peak in the power spectrum $\sigma^2=\langle(\Omega-\langle\Omega\rangle)^2\rangle/\langle\Omega\rangle^2$, calculated by integrating over frequencies in the vicinity of the fundamental component and normalizating by the first moment $\langle\Omega\rangle$. Figure 11(a) shows results of measurements for $R=3.0$ and $z=100$, where the vortex amplitude was saturated. We will show in Sec. VII that broadened spectra reflect a random wandering of the vortex phase that stems from noise amplification. There is a sharp corner and rise in spectral width σ as ϵ is reduced. We located this corner for various R; the results are plotted in the stability diagram Fig. 2 as the upper set of data points. They agree closely with the numerical evaluation of ϵ_a based on the Navier-Stokes equations and given by Eq. (6.1), indicating that the onset of spectral broadening corresponds to the absolute instability boundary ϵ_a.

Simulations of the CGL equation (5.2) support this association. For these simulations, g was set to 1, and *for this section only* noise was modeled by choosing random values for the real and imaginary parts of $A(z=0)$ at each time step, with values uniformly distributed between $\pm n$. The resulting velocity function

$$\Psi=\mathrm{Re}\{A(z,t)\exp[i(k_c z-\Omega_c t)]\}$$

at $z=100d$ closely resembled its experimental counterpart. As shown in Fig. 11(b), the second moment σ^2 undergoes a transition that is also remarkably similar to that seen in the experiment. The location of the transition varied less than $\delta\epsilon=\pm0.005$ for $10^{-9}\le n\le 10^{-3}$, where onset is taken to be the point where σ^2 first departs from its baseline. The vertical dashed line in Fig. 11(b) corresponds to $\epsilon_a^{\mathrm{CGL}}$ (Eq. (5.4)) for $R=3.0$. The onset of spectral broadening is clearly identified with $\epsilon_a^{\mathrm{CGL}}$. Thus spectral broadening is characteristic of patterns in the convectively unstable regime, and the sharp transition in

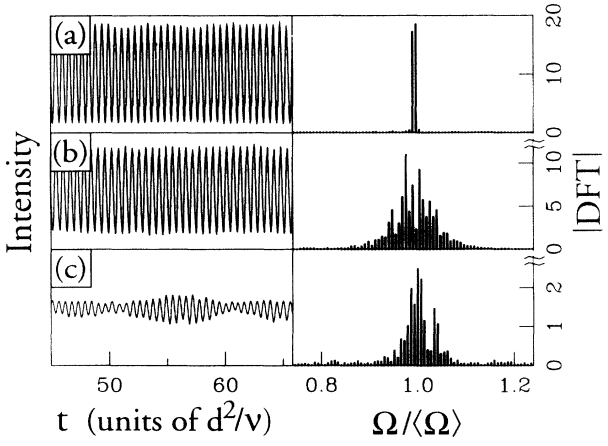

FIG. 10. Time series of reflected light, and their DFT moduli near the fundamental peak, at $z=100$ for $R=3.0$. About $\frac{1}{4}$ of each series is shown. (a) $\epsilon-\epsilon_c=0.0896$. (b) $\epsilon-\epsilon_c=0.0318$. The DFT peak shows considerable broadening. In (c), structure persists at small $\epsilon-\epsilon_c=0.0077$.

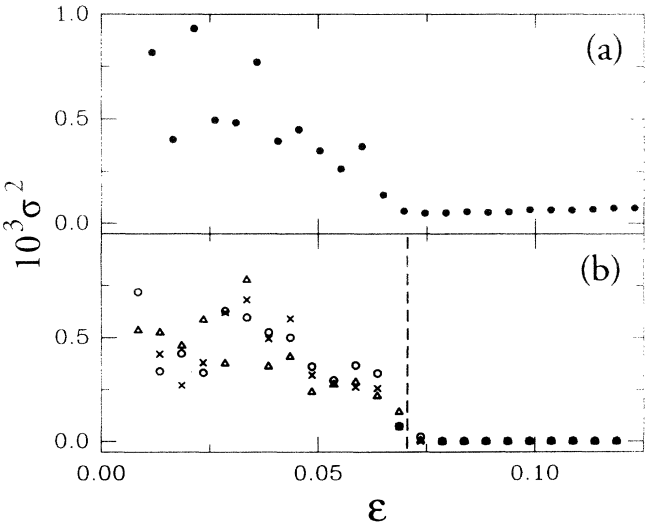

FIG. 11. (a) Normalized second moment of the fundamental peak in the DFT power vs ϵ at $R=3.0$ for experimental time series at $z=100$. The transition at $\epsilon=0.065$ indicates the onset of phase noise. (b) Corresponding results for Eq. (5.2) for inlet noise levels 10^{-6} (+), 10^{-5} (△), and 10^{-4} (○), respectively. The dashed line locates $\epsilon_a^{\mathrm{CGL}}=0.071$.

spectral width provides an excellent diagnostic for locating the stability boundary ϵ_a, even in cases where the noise source or strength is unknown. It would be of interest to test the generality of this signature in other open systems, such as wakes and jets, known to have both convectively and absolutely unstable parameter regimes [15].

VII. NOISE-SUSTAINED PATTERNS

In this section we characterize the noise-sustained patterns observed in the convectively unstable regime $\epsilon_c < \epsilon < \epsilon_a$, and show how they arise from very small amplitude noise through the amplification mechanism of convective instability. Much of the experimental data can be understood in terms of spatial growth in the linearized CGL equation, as well as from simulations of the nonlinear, stochastic CGL Eq. (5.2). The patterns can be succinctly characterized by a vortex phase that executes a pseudorandom walk relative to an average linear increase in time.

A. Observed properties of noise-sustained structure

Basic features of noise-sustained patterns have been shown in Figs. 4 and 7. Again, the amplitude of the secondary flow grows from near zero at the inlet to a fully developed traveling vortex pattern over a characteristic length l_h. In this section we focus on parameter values $\tilde{\epsilon}=0.035$ ($\epsilon=0.039$) and $R=3.0$, near the middle of the convectively unstable regime of Fig. 2, for which $l_h \approx 37$ in the experiment.

Figure 12 shows time series of the axial velocity taken *via* LDV, with mean values subtracted, and corresponding power spectra, at various axial positions. The data for $z < l_h$ show large variations in their oscillation amplitudes, whereas for $z > l_h$ saturation renders the amplitudes nearly constant. (The time series at $z=100$ appears slightly nonuniform on the scale of a few periods due to beating effects produced by sampling only a few points per oscillation.) A slight narrowing of the spectra with increasing z is also apparent. Velocities for $z<15$ approached the experimental resolution and could not be measured effectively. In the next section we will show that the effective noise level is well below the experimental resolution.

The solid oscillating curve in Fig. 13 shows the normalized temporal autocorrelation function of the axial component of the vortex velocity at $z=100$. The flow is not perfectly periodic, but rather loses its correlation over a number of periods. The dotted curve and the envelope are results derived below from the CGL equation.

B. Spatial amplification in the CGL equation

Many of the observed properties can be understood using the linear parts of the CGL equation (5.2) to characterize the amplification of perturbations. Following Deissler [12], the amplitude can be expanded as

$$A(z,t)=\int_{-\infty}^{\infty} d\omega\, A_0(\omega) e^{\beta(\omega)z - i\omega t}. \tag{7.1}$$

Here the frequency ω is real, the wave number β is complex, and both represent deviations from their critical values. One may picture noise or other drive sources at the upstream end $z=0$ having Fourier transform $A_0(\omega)$ which are amplified further downstream. This *spatial* amplification is described by the real part of β. Although the actual noise source may be spatially distributed, this picture is conceptually useful because the noise furthest upstream has the most time to grow before reaching a given axial position. The "spatial" dispersion relation from the CGL equation (5.2) is [12]

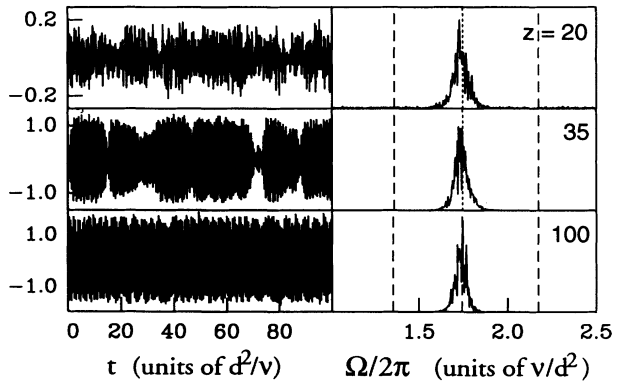

FIG. 12. Time series of the measured axial velocity and scaled power spectra showing their spatial development for (top to bottom) $z=20$, 35, and 100, for $R=3.0$ and $\epsilon=0.0385$ ($\tilde{\epsilon}=0.035$). The dashed lines locate the edges of the CGL growth band $\omega_{\pm}$, and the dotted line is the maximal growth frequency ω_m (see text, Sec. VII B).

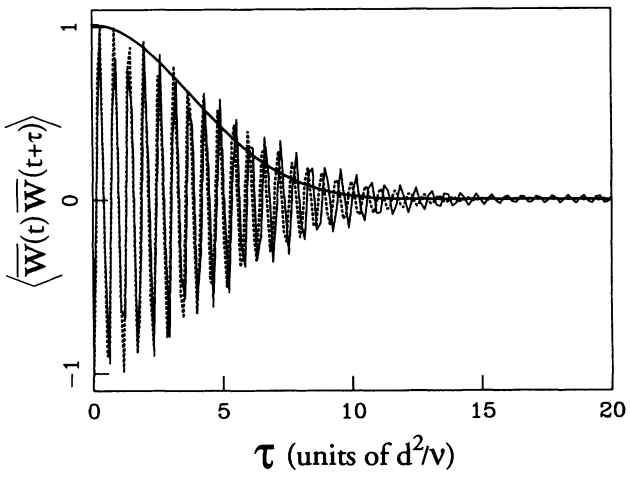

FIG. 13. Normalized temporal autocorrelation function of the axial component of the vortex velocity for $R=3.0$ and $\tilde{\epsilon}=0.035$. The solid oscillating curve is from experiment, and the dotted curve is from the CGL equation with noise level $F_A=4.3\times10^{-9}$, both for $z=100$. The solid envelope is the result from the linearized CGL equation at $z=35$, shown for comparison with the nonlinear state at $z=100$.

$$\beta(\omega)=\frac{s\tau_0-\sqrt{s^2\tau_0^2-4\xi_0^2(1+ic_1)[\tilde{\epsilon}(1+ic_0)+i\omega\tau_0]}}{2\xi_0^2(1+ic_1)} . \tag{7.2}$$

The spatial growth rate β^r and wave number β^i are plotted vs ω in Fig. 14 for $R=3.0$ and $\tilde{\epsilon}=0.035$, with other coefficients taken from the linear stability results of Secs. IV and V. The system responds with spatial growth for the band of frequencies for which $\beta^r>0$. The limits of this band are found by imposing $\beta^r=0$. (Again, ω is real, signifying zero *temporal* growth at a given spatial position.) One obtains $\omega_-<\omega<\omega_+$ with

$$\omega_\pm=(\tilde{\epsilon}/\tau_0)(c_1-c_0)\pm s\sqrt{\tilde{\epsilon}}/\xi_0 .$$

The driving frequency which gives fastest spatial growth is found [60] from $\partial\beta^r/\partial\omega=0$, giving [12] $\omega_m=-(\tilde{\epsilon}/\tau_0)(c_1+c_0)$. The corresponding maximum growth rate

$$\beta_m^r=\beta^r(\omega_m)=\frac{s\tau_0}{2\xi_0^2(1+c_1^2)}[1-\sqrt{1-\tilde{\epsilon}/\tilde{\epsilon}_a^{\mathrm{CGL}}}] \tag{7.3}$$

is plotted in Fig. 15 vs $\tilde{\epsilon}$. These extremal values should dominate in the case of a broadband noise source overlapping ω_m. Indeed, ω_m closely matches the center frequencies of the peaks in the experimental spectra of Fig. 12. Note that spatial growth is defined only in the convectively unstable regime $0<\tilde{\epsilon}<\tilde{\epsilon}_a^{\mathrm{CGL}}$. In the absolutely unstable case, this picture is not relevant because temporal growth occurs at fixed z, i.e., $\omega^i>0$, and β^r is undefined. In that case, the growth of the envelope from zero at the inlet (as in the top frame of Fig. 4) is determined by nonlinear saturation rather than linear amplification.

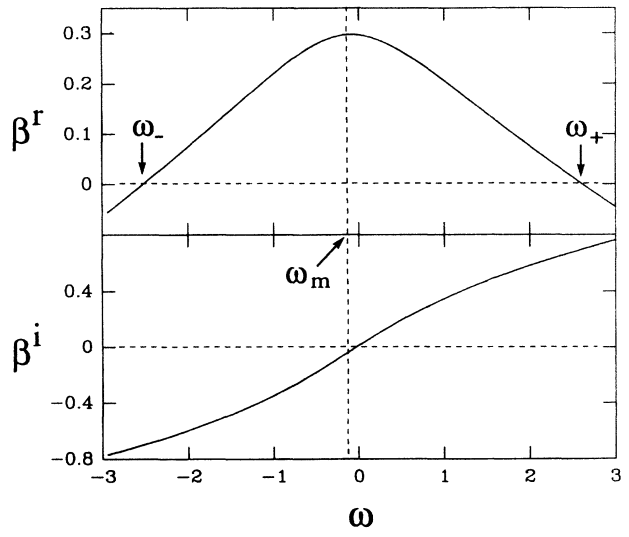

FIG. 14. Spatial growth rate (top) and wave number (bottom) vs frequency in the linearized CGL equation for $R=3.0$ and $\tilde{\epsilon}=0.035$.

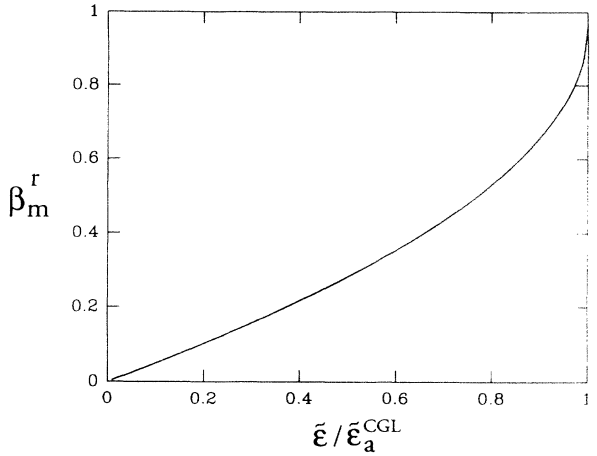

FIG. 15. Maximum spatial growth rate for the linearized CGL equation; $R=3.0$. Note that $\beta_m^r(\tilde{\epsilon}_a^{\mathrm{CGL}})\neq 1.0$.

C. Spatial dependence of the power spectrum

If a convectively unstable system is driven by a broadband noise source, i.e., one which drives the system uniformly over the range $\omega_-<\omega<\omega_+$, the system response depends strongly on axial position. Assuming the noise induces an amplitude response $A_0(\omega)$ having a frequency-independent modulus, the power spectrum of $A(z,t)$ obeys $|A(z,\omega)|^2\propto e^{2\beta^r(\omega)z}$. Thus small disturbances can be amplified enormously for sufficiently large z. For example, with $R=3.0$ and $\tilde{\epsilon}=0.035$, the power of perturbations near $z=0$ with $\omega=\omega_m$ grows by about a factor of $e^{2\beta_m l_h}\approx 10^9$ by $z=l_h\approx 35$, at which point nonlinear terms begin to saturate the growth. Since the spatial growth rate $\beta^r(\omega)$ is frequency dependent, the shape of the power spectrum evolves strongly with z. Frequencies near ω_m are more strongly amplified than others, resulting in spectral narrowing with z, as shown in Fig. 16.

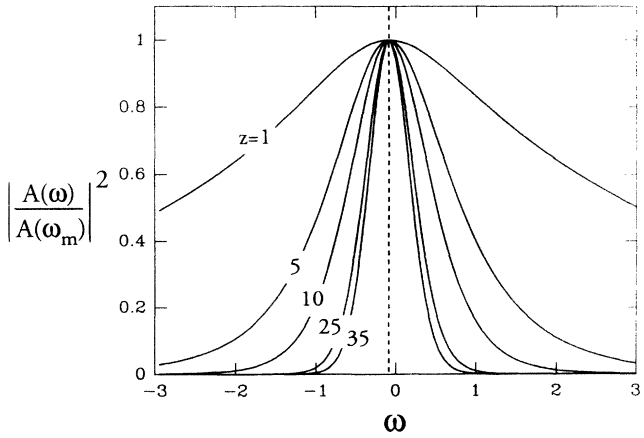

FIG. 16. Spatial development of the spectrum in the linearized CGL equation. Top to bottom: $z=1,5,10,25,35$. The maximal growth frequency ω_m is marked by the dashed line.

The Fourier transform of the spectral shape $e^{2\beta^r(\omega)z}$ with respect to ω gives the temporal autocorrelation function of the amplitude, shown as the solid envelope in Fig. 13. This linearized picture is valid up to only $z=l_h\approx 37$. The corresponding autocorrelation time is slightly smaller than that measured at $z=100$ (and that of the numerical CGL result described below), most likely because spectral narrowing continues in the nonlinear regime by phase diffusion.

Numerical integration of the CGL equation (5.2) shows how the amplification acts on noise-induced perturbations. Using spatially distributed white noise as in Eq. (5.10), the velocity function

$$\Psi=\mathrm{Re}\{A(z,t)\exp[i(k_c z-\Omega_c t)]\}$$

was generated vs time for various axial positions z. For the results shown here, the nonlinear coefficient g was set to 0.000 835 and the noise power to $F_A=4.3\times10^{-9}$, as motivated in the next section.

The time-averaged profile of the velocity function, $\langle\Psi^2(z)\rangle^{1/2}$, is shown in Fig. 17. The profile grows from an extremely small value near $z=0$ determined by the noise level to a saturated value close to $\sqrt{\tilde{\epsilon}/2g}$ at large z, an amplification of 10^5 in amplitude or 10^{10} in power. The characteristic growth length $l_h\approx 37$, as in the experiment. Figure 18 shows time series of the velocity function at various positions z together with their spectra. As in the experiment (Fig. 12), the velocity functions for $z<l_h$ show large variations in their amplitude, whereas for $z>l_h$ saturation renders the amplitudes nearly constant. Spectral narrowing is very evident. The spectral properties correspond closely to the analytic results for the growth band limits $\omega_-/2\pi=-0.40$ and $\omega_+/2\pi=0.42$, and maximal growth frequency $\omega_m/2\pi=-0.01$, giving $\beta_m=0.298$.

The dotted curve in Fig. 13 shows the temporal autocorrelation function of the CGL velocity function at $z=100$. The solid envelope is again the result from the linearized CGL equation for $z=l_h=35$. The correlation

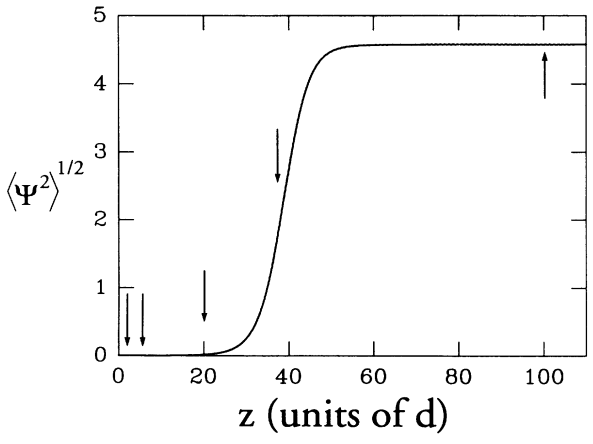

FIG. 17. Time-averaged root-mean-square velocity function obtained by integrating the stochastic CGL equation; $R=3.0$, $\tilde{\epsilon}=0.035$. Arrows mark the locations of time series used in Fig. 18.

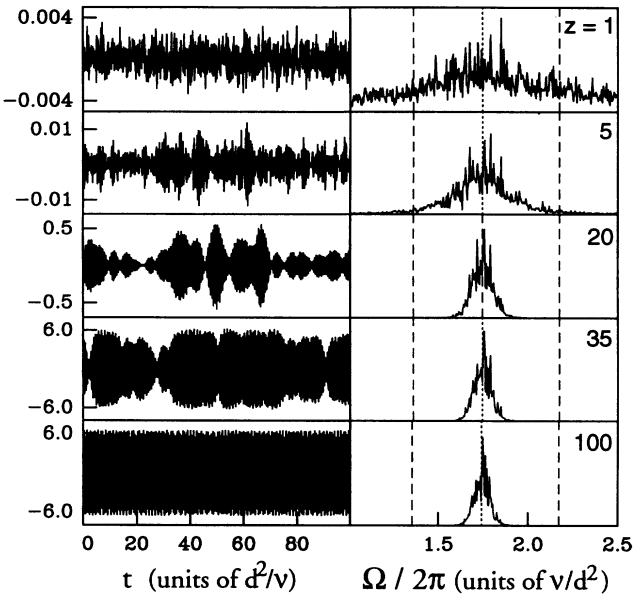

FIG. 18. Spatial development of the velocity function and its power spectrum in the stochastic CGL equation at (top to bottom) $z=1,5,20,35,100$ for $R=3.0$, $\tilde{\epsilon}=0.035$, and noise level $F_A=4.3\times10^{-9}$. The CGL growth band limits $\omega_\pm$ are shown as dashed lines and the maximal growth frequency ω_m by the dotted line.

time, here defined as the time lag at which the autocorrelation function drops to half maximum, agrees well with the experimental result shown as the solid oscillating curve. We do not have an explanation for the slight frequency difference between the experiment and simulation.

In sum, the CGL equation shows quantitatively how broadband noise near the inlet is amplified and spectrally narrowed, leading to a macroscopic traveling vortex pattern correlated over several vortices.

D. Pseudorandom phase walk

The fully developed traveling vortex patterns can be succinctly characterized *via* their phase [21]. We write the velocity time series as $v=B(t)e^{-i\Omega_d t}+\text{c.c.}$, where $B(t)=|B(t)|e^{i\phi(t)}$. The frequency Ω_d is chosen so that $\int_0^T\phi(t)dt=0$, thus removing as much of the fast variation as possible from the complex amplitude $B(t)$. For $z\gg l_h$, the amplitude is saturated ($|B|\approx$const) and the features of interest reside in the phase $\phi(t)$, which represents the deviation of the vortex phase from that of a perfectly periodic signal of frequency Ω_d.

To extract the phase, we demodulated the time series by removing the peak in the DFT at $-\Omega_d$ and shifting the peak at Ω_d to zero frequency. Inverting then yielded $B(t)=|B|e^{i\phi(t)}$. Assuming $|B|=$const (an approximation good to within a few percent for large z, as shown below), $\phi=\tan^{-1}[\mathrm{Im}(B)/\mathrm{Re}(B)]$. The demodulation frequency Ω_d is adjusted until $\int_0^T\phi(t)dt=0$. In all cases we examined, Ω_d was within a few percent of $\Omega_m=\Omega_c+\omega_m$.

Figures 19 and 20 show the results of this procedure for CGL integrations and experiment, respectively, with parameters again $\tilde{\epsilon}=0.035$ ($\epsilon=0.039$), $R=3.0$, and $z=100$. In the experiment, the viscosity was 0.059 S. In the simulations, $F_A=4.3\times10^{-9}$, and $g=0.000\,835$. The modulus $|B|$ is shown in parts 19(a) and 20(a) over several thousand oscillations. It is nearly constant in time, yet the real part of the amplitude in (b) reveals an irregular time variation which can be traced to the time variation of the phase ϕ in parts (c). The time derivative shown in parts (d) gives the local deviation from the mean frequency, $d\phi/dt=\Omega-\Omega_d$. The phase can thus be viewed as an accumulation of random, bounded fluctuations in the frequency, and so might be expected to resemble a random walk.

Figure 21 shows the rms deviation of the phase ϕ from its mean of zero vs the duration of the time series T, averaged over several time series for experiment and CGL simulations. In both cases, the deviation obeys a power law $\langle\phi^2\rangle^{1/2}\propto T^{\alpha}$ with $\alpha=0.59\pm0.015$. Further CGL simulations showed that both the exponent [61] and magnitude of the deviations are insensitive to the values of the imaginary coefficients c_i, and to the magnitude of the noise level, for noise powers up to two decades greater and less than the value used to generate the results of Fig. 21. The value $\alpha>0.50$ suggests a process with "persistence," analogous to the time series of many natural processes [62], although the mechanism responsible in the present case is unclear. It is interesting that such an "anomalous" exponent (differing from the simplest random walk value $\frac{1}{2}$) arises in a truly one-dimensional system, as evidenced by its appearance in the one-dimensional CGL equation. Also striking is the fact that the exponent α does not depend on the noise level in the simulations.

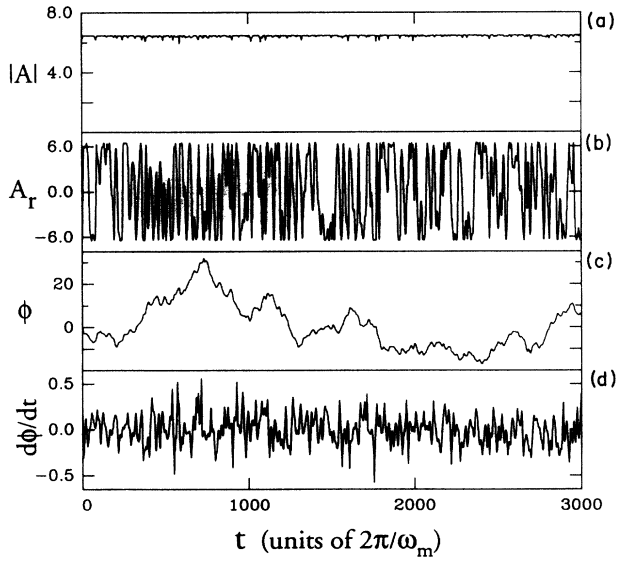

FIG. 19. Demodulation of the velocity function in the CGL equation at $z=100$ for $R=3.0$, $\tilde{\epsilon}=0.035$, and $F_A=4.3\times10^{-9}$. Shown top to bottom are the modulus, real part of the amplitude, phase, and phase derivative vs time.

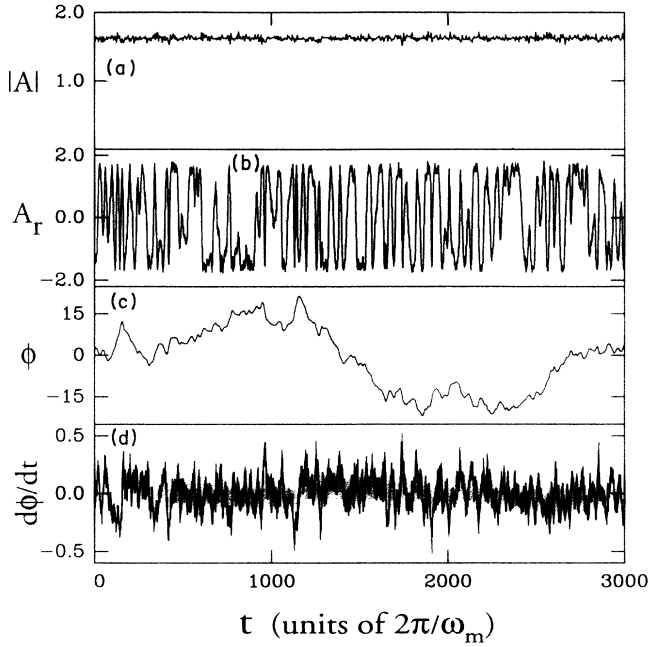

FIG. 20. Same as Fig. 19, but for experimental LDV measurements, with the same R and $\tilde{\epsilon}$, and $\nu=0.059$ S.

VIII. NOISE PROPERTIES

Quantitative knowledge of stability properties and the amplification mechanism, in combination with the CGL equation (5.2) for which the noise strength is the only adjustable parameter, allow us to determine the power of the experimental noise. We compare the results with theoretical predictions for thermal noise.

A. Noise magnitude

Figure 22 shows amplitude profiles for $R=3.0$, kinematic viscosity $\nu=0.059$ S, and various ϵ. In the experi-

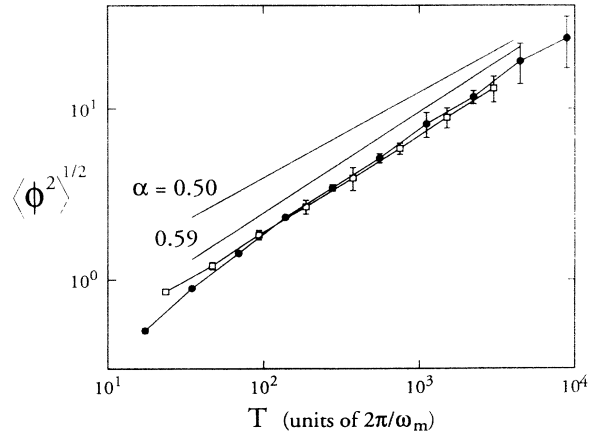

FIG. 21. rms deviation of the phase from its mean of zero vs the length of the time series, for $R=3.0$, $\tilde{\epsilon}=0.035$, and $z=100$. Circles are for experiment, squares from CGL integrations with $F_A=4.3\times10^{-9}$. Straight lines compare power law exponents.

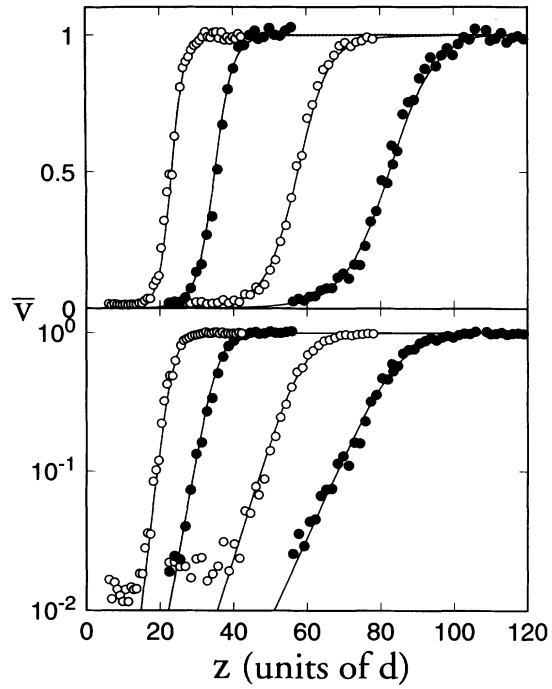

FIG. 22. Normalized velocity profiles $\bar{v}(z)$ from experiment (data points) and CGL simulation (curves) for $R=3.0$ and viscosity $\nu=0.059$ S. Left to right: $\tilde{\epsilon}=0.055$, 0.040, 0.025, 0.0175 ($\epsilon=0.059$, 0.044, 0.029, 0.021). In the top half, $\bar{v}(z)$ is given on a linear scale. The bottom half shows the same data on a logarithmic scale and reveals the initial exponential increase of $\bar{v}(z)$ with z. A single noise level $F_A=4.3\times10^{-9}$ was used in the simulations.

ment, a LDV time series covering at least several hundred periods was recorded at an axial position and the rms deviation of the axial velocity from its time average determined. Measurements were repeated at a number of axial positions. For the plots of this section, rms velocities were normalized by their saturated values at large $z\gg l_h$ to produce a scaled velocity profile $\bar{v}(z)$. In the top half of the figure, $\bar{v}(z)$ is given on a linear scale. The logarithmic plot of the bottom half shows the saturation at small $\bar{v}(z)$ because of the experimental noise floor, as well as the initial exponential increase of $\bar{v}(z)$ with z. As in Fig. 4, the healing length l_h increases as ϵ is decreased.

We estimated the noise strength by comparing the measured profiles $\bar{v}(z)$ with those of

$$A_{\rm av}=\langle |A(z,t)|^2\rangle^{1/2}$$

where the angular bracket indicates a time average. Here $A_{\rm av}$ was generated numerically from the stochastic CGL equation (5.2), for which all coefficients are known. For comparison with $\bar{v}(z)$, $A_{\rm av}$ was divided by the saturation value $|A_{\rm av}(\infty)|\approx(\tilde{\epsilon}/g)^{1/2}$. The noise strength F_A was adjusted until the profiles matched the data. It is important to note that the value of F_A obtained from this comparison depends upon the normalization of A, which in turn is determined by the value of g. Specifically, the same profiles $A_{\rm av}/|A(\infty)|$ are obtained for various g if F_A is changed in proportion to $1/g$. We used $\tilde{\epsilon}$ corresponding to experiment, and set $g=g_0=0.000\,835$ as found in Sec. V A. This assures that the amplitude scale is correctly related to the physical velocities by Eq. (5.1). (We ignored the small R dependence of g_0.) A single noise level

$$F_A(\nu=0.059\ \text{S})=4.3\times10^{-9}$$

produced the solid curves in Fig. 22, which closely match the experimental data for each ϵ.

A fit to the data at a given ϵ yields a small uncertainty for F_A due to the scatter in the velocity data. However, errors in F_A due to uncertainties in ϵ are larger. On the basis of systematic deviations of data at a given ϵ from the curves in Fig. 22 (which are too small to be obvious on the scale of that figure) we estimate that the uncertainty in F_A is about a factor of 1.5 or 2. In addition, there are possible systematic errors associated with entrance-length effects discussed in Sec. VIII B below, yielding a total uncertainty in F_A of about a factor of 3.

In order to illustrate the smallness of the noise level F_A, we estimate the physical velocity fluctuations which would be induced by such a noise level in the system without through-flow and below the onset of Taylor vortices. We use Eq. (5.1) to give the amplitude of the dimensioned axial velocity

$$\tilde{W}(r)=2(\nu/d)|A(z,t)||w(r)|\ ,$$

where $w(r)$ is the axial component of the radial eigenfunction obtained from linear stability analysis. For $\tilde{\epsilon}<0$, Eq. (5.2) gives for the magnitude of the velocity fluctuations

$$\langle\tilde{W}^2\rangle=4(\nu^2/d^2)|w|^2(F_A/2|\tilde{\epsilon}|^{1/2})\ . \tag{8.1a}$$

To achieve a specific comparison, we set $\tilde{\epsilon}=-1$, corresponding to no rotation. Although the amplitude-equation description can be expected to be valid only for small $\tilde{\epsilon}$, this choice approximates the equilibrium state and also gives a crude estimate for the conditions near the inlet of the apparatus where the flow has no rotation. Using $|w(r_m)|=0.30$ as in Sec. V A, and $\nu=0.059$ S as in Fig. 22, gives

$$\sqrt{\langle\tilde{W}^2\rangle}=0.024\ \mu\text{m/s}\ . \tag{8.1b}$$

This may be compared to typical velocities in the fully developed vortex flow at large $z\gg l_h$:

$$\tilde{W}_{\rm sat}=2(\nu/d)|w|\sqrt{\tilde{\epsilon}/g}\ , \tag{8.2}$$

which for a typical value $\tilde{\epsilon}=0.035$ gives $\tilde{W}_{\rm sat}=0.34$ cm/s, about 10^5 times larger than the rms noise velocities.

B. Effect of entry length

To be precise, we should account for the entry length of the base flow when using amplitude profiles to estimate the noise magnitude. Fluid enters the apparatus with no rotation, and requires some (typically small) streamwise

distance l_e to acquire the Couette rotation profile. The entry length depends on R: at larger R the fluid can move a greater distance in the time required to acquire rotation. The entry length is apparent in Fig. 3, in which a pulse of Taylor vortices initially decays upon entering the upstream end of the apparatus [63], indicating that the fluid has not reached full rotation and that effectively $\epsilon<0$. In effect, ϵ increases from -1 at $z<0$ to its asymptotic value near $z=l_e$. Simulations of the CGL equation could in principle account for this, with the result that the numerical profiles would be shifted further downstream for given parameters and noise strength, and that the estimate of the experimental noise level would increase accordingly.

At the small Reynolds numbers considered here, we find this shift to be small. Precise measurement of the azimuthal component of the base flow is problematic close to the inlet. Another method for estimating the length l_e is to measure the amplitude profiles in the *absolutely* unstable regime $\epsilon>\epsilon_a$. In that case the flow is insensitive to noise, and the noise strength is removed as a parameter. Comparing profiles in experiment and simulation gives a relative axial shift which can be used as a measure of the entry length for the convectively unstable regime. Such measurements at $R=3.0$ indicate a shift of at most 1.5.

To estimate the noise power that would be inferred if the entry region were taken into account, we can use the spatial growth rate β_m^r to calculate the factor by which the mean-squared fluctuations of the amplitude increase over the distance l_e. This factor should be a reasonable estimate of the increase in noise power required to generate the same (measured) downstream amplitude, well away from the entry region. The result is $F_A'\approx F_A e^{2\beta_m^r l_e}\approx 1.8F_A$ using the measured profile shift $l_e\approx 1.5=z_1-z_2$ and $\beta_m^r=0.20$ ($R=3.0$, $\bar{\epsilon}=0.025$).

C. Thermal noise magnitude

We naturally would like to compare the noise level $F_A\simeq 4.3\times 10^{-9}$ found in the experiment (Sec. VIII A) to the thermal noise level $F_A^{\rm th}$. A simple order of magnitude comparison can be made between the vortex flow velocity corresponding to the experimental noise level [0.024 μm/s, Eq. (8.1b)], and the root-mean-square thermal velocity of the center of mass of a fluid element having the volume of one vortex:

$$(6k_BT/\rho\pi^2\bar{r}d^2)^{1/2}=0.0016\ \mu\text{m/s}\ ,$$

about a factor of 15 smaller. This corresponds to a factor of 225 in noise power (which is proportional to F_A), but this comparison can only be regarded as approximate.

More detailed theoretical treatments of stochastic hydrodynamics [11] account for random molecular motion by adding a Langevin noise term $\vec{\nabla}\cdot\mathbf{S}$ to the right-hand side of the (dimensionless) Navier-Stokes equations (4.2a). The stochastic part of the stress tensor has a Gaussian distribution and correlations [11]

$$\langle S_{ij}(\vec{x},t)S_{lm}(\vec{x}',t')\rangle=(2k_BT/\rho d\nu^2)\delta(\vec{x}-\vec{x}')\delta(t-t')\times(\delta_{il}\delta_{jm}+\delta_{im}\delta_{jl})\ , \tag{8.3}$$

which assures that a closed system will relax to thermodynamic equilibrium, and there will display fluctuations of the proper amplitude. The noise power contains a characteristic ratio of the microscopic thermal energy k_BT to the macroscopic energy [64] $(\rho d^3)(\nu/d)^2$, which is approximately the energy of a fluid element of volume d^3 for the developed flow. This ratio is very small in macroscopic systems (about 10^{-11} for our case), so that thermal noise cannot normally affect a developed flow. This is not the case, however, for flows very near threshold, or for systems for which the characteristic dimensions are sufficiently small. Recently, experimental attention has been given to exploring situations where stochastic effects are observable in pattern-forming systems [29–31,65].

Considerable effort has been devoted to carrying the noise term through to reduced dynamical equations such as the amplitude equation Eq. (5.2) that describe *nonequilibrium* systems [13,27,55,56,66–69]. In doing so, the assumption is made that the equilibrium expression for the noise correlations Eq. (8.3) remains valid near threshold since the macroscopic dynamics are relatively slow. An example is the Swift-Hohenberg [13,56] equation describing convection, in which thermal velocity fluctuations produce a real noise term which we used in earlier work to compare to the experimental noise we observe in the Taylor-Couette system [21,70]. A calculation of the noise power $F_A^{\rm th}$ in Eq. (5.10) specific to the Taylor-Couette geometry (but for $R=0$) was done recently by Swift, Babcock, and Hohenberg [27] with the result

$$F_A^{\rm th}=\frac{\tau_0 k_BT}{2\pi\xi_0\rho d\nu^2}I\ , \tag{8.4a}$$

with

$$I=[N_1(k_c)N_1(-k_c)]^{-1}\times\int_{r_1}^{r_2}\left[k_c^2|v^\dagger|^2+\left|-ik_cu^\dagger+\frac{d}{dr}w^\dagger\right|^2+\frac{1}{r^2}\left|\frac{d}{dr}(rv^\dagger)\right|^2\right]r\,dr\ . \tag{8.4b}$$

Here, $\vec{V}^\dagger=(u^\dagger,v^\dagger,w^\dagger)$ is the radial eigenfunction of the adjoint eigenvalue problem at critical parameter values, and N_1 is the overlap of the regular and adjoint eigenfunctions $N_1=\int_{r_1}^{r_2}\vec{V}^\dagger(r)\cdot\vec{V}^*(r)r\,dr$. Equations (8.4) hold for the case of no through-flow [27,71]. Note that I depends on η, but not on r_1 and r_2 separately, as these have been scaled by the gap $d=\bar{r}_2-\bar{r}_1$.

It is worth noting that once a relationship between physical velocity, the amplitude A, and the eigenfunction $w(r)$ has been defined, and a normalization chosen for the eigenfunctions, the nonlinear coefficient g in the CGL equation is fixed. Again, we used Eq. (5.1), scaled velocities by ν/d, and chose a normalization $\int_{r_1}^{r_2}\vec{U}(r)\cdot\vec{U}^*(r)r\,dr=1$. This fixed $g=0.000\,835$, as found in Sec. V A.

Using the methods of Sec. IV B, we numerically evaluated the adjoint eigenfunctions and their normalizations

at onset for $\eta=0.738$ and found [72] $N_1=0.416-0.774i$ and $I=40.57$. With $\tau_0=0.038$, we find

$$F_A^{\text{th}}=1.6\times10^{-11}$$

for $\nu=0.059$ S and $d=0.677$ cm, about 270 times smaller than the experimental value determined in Sec. VIII A. A similar conclusion has been reached recently by Deissler [68] from numerical simulations. Since the rms velocity fluctuations vary as $F_A^{1/2}$ [see Eq. (8.1a)], the thermal fluctuations in the axial velocity are about $\sqrt{270}\approx16$ times smaller than the experimental value 0.024 μm/s, or

$$\sqrt{\langle \tilde{W}_{\text{th}}^2 \rangle}\simeq0.0015\ \mu\text{m/s}\ . \tag{8.5}$$

This result is remarkably close to the naive estimate of a factor of 15 made at the beginning of this section.

D. Comparison with our previous work

In two previous publications [20,21] we presented results for noise-sustained structures which were obtained with Kalliroscope flow visualization rather than with LDV, but in the same apparatus as the one used for the present work. We can combine those results with the current work to determine how the experimental noise compares with thermal noise calculations for a range of Reynolds numbers R.

Measurements of the minimum value $\tilde{\epsilon}_s$ at which sustained patterns are first detectable were made at three axial positions $z=25$, 50, and 100 and for various R (see Fig. 6 of Ref. [20] or Fig. 1 of Ref. [21]). This was done by taking time series of the optical signal at various $\tilde{\epsilon}$, Fourier transforming the series, and extrapolating the power under the Fourier peak to zero. We estimate the experimental uncertainty in $\tilde{\epsilon}_s$ to be no larger than ±0.002.

A link to our current work can be made by using the CGL equation to determine the amplitude $A_{\text{av}}^{\text{min}}$ that corresponds to $\tilde{\epsilon}_s$ for $R=3$. We integrated the stochastic GL equation, using the $\tilde{\epsilon}_s$ values 0.0304, 0.0170, and 0.0074 found in Ref. [20] for $z=25$, 50, and 100, respectively, and for $R=2.99$. The fluid viscosity in that work was 0.025 S, i.e., a factor of 0.025/0.059 smaller than for the data in Fig. 22. Since F_A varies as $1/\nu^2$ (see also Sec. VIII F below), our present work implies a noise power $F_A(\nu=0.025\ \text{S})=2.4\times10^{-8}$. This value was used in the integrations. The results for A_{av} are shown in Fig. 23. The vertical dashed lines correspond to the axial positions of the measurements of $\tilde{\epsilon}_s$, and their intersections with the corresponding $A_{\text{av}}(z)$ yield the detectability limit. Based on the results for $z=25$ and 50, we adopt a value [73] $A_{\text{av}}^{\text{min}}=0.06$ for the analysis of the experimental $\tilde{\epsilon}_s$ values at all R. It is shown as the horizontal dash-dotted line in Fig. 23. The measurements at $z=100$, which give $A_{\text{av}}^{\text{min}}=0.04$, are somewhat less accurate because the value of ϵ_s is small and its relative uncertainty rather large. Setting $\sqrt{\tilde{\epsilon}/g_0}\simeq A_{\text{av}}^{\text{min}}=0.06$ in the last equation of Sec. V A, we have $W=0.036$, which with $\nu/d=370$ μm/s gives 13 μm/s as an estimate of the smallest detectable velocity amplitude.

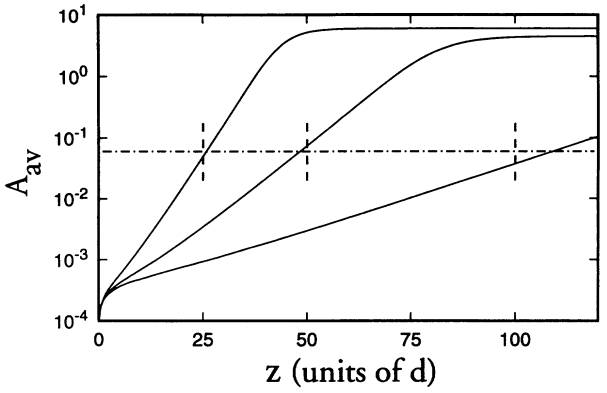

FIG. 23. Root mean square of the modulus of A, on a logarithmic scale, as a function of the axial position z for (from left to right) $\tilde{\epsilon}=0.0304$, 0.0170, and 0.0074 and for $R=2.99$. The vertical dashed lines are the axial positions at which the $\tilde{\epsilon}_s$ values were determined for the detection of noise-sustained structure with Kalliroscope. The dash-dotted horizontal line is the detectability limit which was adopted for further data analysis.

Using the values ϵ_s measured at various z and R in the previous work, we can now determine the Reynolds number dependence of the noise power in that experiment. The noise power F_A was adjusted in the integration of the stochastic CGL equation until $A_{\text{av}}(\tilde{\epsilon}_s,z,R)=A_{\text{av}}^{\text{min}}=0.06$. Since F_A depends on the gap d and the viscosity ν of a particular experiment, a direct comparison of experimental values for F_A is not very illuminating. More revealing is the ratio F_A/F_A^{th}, which is independent of d and ν. Figure 24 shows this quantity as solid circles [74], with $F_A^{\text{th}}(\nu=0.025\ \text{S})=8.4\times10^{-11}$. The horizontal solid line corresponds to our present best value $F_A/F_A^{\text{th}}=270$, based on the LDV measurements

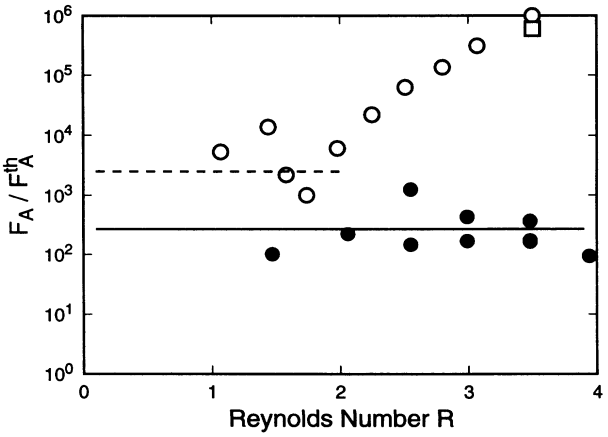

FIG. 24. Ratios of experimental noise power to theoretical predictions of thermal noise power. Open circles correspond to the data of Ref. [26], and solid symbols to the present work. The solid horizontal line represents the best fit to the data in Fig. 22. The horizontal dashed line is the plateau value quoted by Tsameret, Goldner, and Steinberg (Ref. [26]).

shown in Fig. 22. The error bars for all the points overlap this best value, which we believe to be accurate to within a factor of 3 or so. Thus, within the resolution of the Kalliroscope data of Refs. [20] and [21], there is no dependence of the noise level in the experiment on Reynolds number for $R \leq 4$.

In the previous publication [21] we quoted an estimate of a noise amplitude $\sigma_n = (2.5 \pm 1.5) \times 10^{-6}$ for $\nu = 0.025$ S, which is related to F_A by

$$\sigma_n = (2\tau_0 \xi_0 g F_A)^{1/2} . \tag{8.6}$$

The quoted value of σ_n was obtained from CGL simulations using $g = 1$. Had they been carried out with $g = 0.000\,835$, the result would have been larger by $(1/0.000\,835)^{1/2}$, giving $\sigma_n = (8.6 \pm 5.2) \times 10^{-5}$. Our present value of $F_A(\nu = 0.025$ S$) = 2.4 \times 10^{-8}$ yields $\sigma_n = 2.2 \times 10^{-5}$, somewhat below the previously quoted lower limit. Our previous conclusion that σ_n was of the order of thermal noise was erroneous because we did not allow for $g \neq 1$ in comparing with thermal noise estimates, and because of the extreme sensitivity of Kalliroscope methods which we did not fully appreciate when comparing the experiment to the CGL equation (Fig. 2 of Ref. [21]).

E. Comparison with work by others

Recently, the noise intensity in a Taylor-vortex system with through-flow was examined by Tsameret, Goldner, and Steinberg (TGS) [26]. Their radius ratio was 0.77, which differs only slightly from ours. Thus it is a good approximation to use the parameters $\tau_0 = 0.037$ and $\xi_0 = 0.27$ (which we presented above in Sec. V A) for the calculation of their thermal noise intensity. Their viscosity was 0.03 S, and the gap between their cylinders was 0.95 cm. With these parameters we find from Eq. (8.4a) the thermal noise intensity $F^{\text{th}}_{A,\text{TGS}} = 4.4 \times 10^{-11}$.

Although the authors present several different ways of analyzing their data, we find it difficult to make a direct comparison with their derived measures of their noise amplitudes. They compare some of their results with numerical integrations of Eq. (5.2) with $f_A = 0$, but with fluctuating boundary values $A(z=0)$ with a Gaussian distribution and a variance $\sigma^2_{n,B}$ rather than with spatially distributed noise $f_A(z,t)$ with correlations given by Eq. (5.10). From numerical studies of Eq. (5.2) they find empirically, for their parameter values, that

$$\sigma_{n,B} \simeq \sigma_n$$

(see Fig. 2 of Ref. [26]), where in our notation σ_n is given by Eq. (8.6) (note that our $\sigma_{n,B}$ is called σ_n by TGS). However, it is known that the relationship between $\sigma_{n,B}$ and σ_n is in general quite complicated. It has been discussed in detail by Swift, Babcock, and Hohenberg [27] (see in particular Sec. IV of that paper). A further complication is that the most detailed analysis provided by TGS consists of a fit of their data for a time average of the measured velocity amplitudes to a *deterministic* integration of a *time average of the amplitude equation* [their Eq. (8)], adjusting the boundary value $\hat{V}_0$ so as to fit the data. They derive a relationship between $\hat{V}_0$ and $\sigma_{n,B}$ from separate measurements as a function of externally injected noise. It is given by Eq. (9) of Ref. [26]. However, one of the authors suggested [75] to us that this relationship is not very accurate.

One unambiguous way for comparison with the data of TGS remains. In their Fig. 13, they show measurements of the time average of the velocity as a function of axial position for $R = 3.5$ and $\tilde{\epsilon} = 0.0367$. We reproduce these measurements in Fig. 25, together with a fit of Eq. (5.2) to them which was carried out in the same way as the fits to our results in Fig. 22. We obtained $F_{A,\text{TGS}}(\nu = 0.03$ S$) = 2.5 \times 10^{-5}$, corresponding to $\sigma_n = 2.07 \times 10^{-5}$. The value of $F_{A,\text{TGS}}$ derived from the experiment exceeds the thermal noise $F^{\text{th}}_{A,\text{TGS}}$ by a factor of about 6×10^5. This ratio is shown in Fig. 24 by the open square. Also shown in Fig. 25, as dashed lines, are solutions of Eq. (5.2) with F_A larger and smaller by a factor of 2 than the best-fit value. These curves illustrate that the precision of the determination of F_A (σ_n) is better than a factor of 2 (1.4). For comparison, we show the results of Fig. 22 for $F = 3.0$ and $\tilde{\epsilon} = 0.040$ (see Fig. 22) as solid squares. The line going through these points is the fit to our data in Fig. 22, which corresponds to $F_A = 4.3 \times 10^{-9} = 274 F^{\text{th}}_A$.

For the data in their Fig. 13, TGS obtained a value of $\hat{V}_0 = 2.7 \times 10^{-5}$ cm/s. Assuming proportionality between $\hat{V}_0$ and σ_n as was done by TGS, we find from the above the calibration

$$\hat{V}_0 / \sigma_n = 1.3 \text{ cm/s}$$

which is in good agreement with Eq. (9) of TGS and their observation that $\sigma_n \simeq \sigma_{n,B}$. Now we have somewhat greater confidence in using the numerical factor in Eq. (9) of TGS for a further analysis of their results.

Further comparison with the data of TGS is possible only under the assumptions that the empirical relationship Eq. (9) of Ref. [26] holds, and that $\sigma_{n,B} \simeq \sigma_n$ as suggested by the data in Fig. 2 of Ref. [26]. We showed

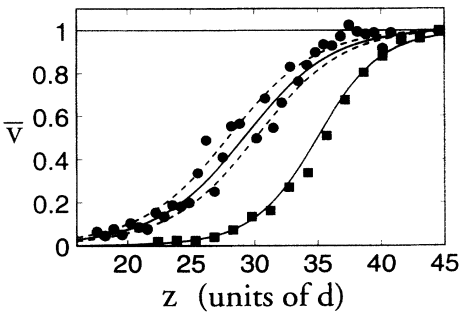

FIG. 25. Normalized velocity profiles $\bar{v}(z)$ from experiment (data points) and CGL simulation (curves). The solid circles are from Fig. 13 of Ref. [26], and are for $R = 3.5$ and $\tilde{\epsilon} = 0.0367$. The solid line through them is a fit of Eq. (5.2) to these data which yielded $F_A = 2.5 \times 10^{-5}$. The dashed lines are for noise intensities a factor of 2 larger and smaller than this best-fit value. For comparison, data from Fig. 22 for $\tilde{\epsilon} = 0.040$ are shown as solid squares. The line through them is the same fit as in Fig. 22 ($F_A = 4.3 \times 10^{-9}$).

above that both of these assumptions seem to be well satisfied for $R=3.5$; but they have to hold over the entire experimental range of R. In their Fig. 14, TGS show values of $\hat{V}_0$ as a function of R. We converted these data to $\sigma_{n,B}$, using Eq. (9) of Ref. [26], took $\sigma_{n,B}$ to be equal to σ_n, and obtained the noise intensity F_A used in the present paper from $F_A=(\sigma_n)^2/(2\tau_0\xi_0 g)$. Here we need to divide by the value $g=0.000\,835$ because it corresponds to the normalization used in the theoretical noise estimate and because TGS used $g=1$ in their fits. We plotted $F_A/F_A^{\rm th}$ for the TGS data in Fig. 24 as open circles. As pointed out by TGS, their noise intensity at large R increases with R. At large R, the results agree well with the open square which we derived from the data in Fig. 13 of Ref. [26] as described above. TGS believe that, for $R\leq 2$, their data become independent of R at a value corresponding to $\hat{V}_0=2\times10^{-6}$ cm/s. Such a "noise floor" would correspond to $F_A/F_A^{\rm th}\simeq 2500$ for their experiment, and is given in Fig. 24 as a horizontal dashed line. It is an order of magnitude larger than our R-independent noise level.

F. Noise spectrum

In addition to the magnitude, one can test the relevance of thermal noise by examining the dependence of $F_A\propto k_BT/(\rho d\nu^2)$ on experimental parameters. It is difficult to produce an observable change in the amplitude profiles by varying the temperature, since the characteristic lengths l_h are only logarithmically dependent on the noise strength, and a sufficient temperature change is impractical while keeping other experimental parameters constant. Instead we probed the stronger dependence on kinematic viscosity ν, which varies with the relative concentrations of water and glycerine in the working fluid.

Figure 26 shows amplitude profiles for $R=3.0$ and $\bar{\epsilon}=0.025$ ($\epsilon=0.029$) and various viscosities. The experimental and CGL simulation profiles were generated in the same way as for Fig. 22. The viscosities were 0.011, 0.016, 0.059, and 0.105 S, which cover a range of glycerine concentrations from 5% to 60% and of time scales $4.4<d^2/\nu<42.0$ s. Figure 27 shows that the noise levels $\sqrt{F_A}$ required to fit the data of Fig. 26 are indeed linear in $1/\nu$.

Nonthermal noise, such as certain types of boundary noise, may also give a $1/\nu$ dependence since the velocity in the CGL equation (5.2) is scaled by ν/d. However, the $1/\nu$ form holds for a decade in frequency, indicating that the relevant experimental noise is "white" over at least a decade. This would seem to rule out many obvious noise sources, such as pump vibration, mechanical resonances, and other sources which tend to be spectrally narrow.

As a check, we varied several experimental features that seemed candidates for the noise source. For example, we changed cylinder motors, pumps, and details of the flow distributor (Fig. 1), the last of which could produce fluctuations in the incoming fluid velocity. In no instance did we observe a change in the apparent noise level.

It may not be too surprising that many common noise sources are unimportant with regard to amplification. The relevant noise must meet two conditions: its spectral content must overlap the bandwidth of amplified frequencies (i.e., it must contain power near ω_m), and its spatial variation must be such that it couples to the traveling modes Eq. (4.3). Many obvious candidates fail the first test since the range of amplified frequencies in our experiments was roughly $0.04<\tilde{\omega}_m/2\pi<0.4$ Hz, much lower than, for example, typical pump or motor resonances. The second condition rules out, for example, rigid, nonrotational vibration of the entire apparatus.

To sum up, the magnitude of the experimental noise is independent of Reynolds number R for $1.5\lesssim R\lesssim 4$, and is a factor of 270 larger than the current best theoretical estimates for thermal noise. It has a "white" spectrum over at least one decade in frequency. The source of the noise is at present unclear. The characteristic growth lengths are only logarithmic in the noise amplitude. Thus, even if the noise source in the experiment were comparable to the thermal levels predicted by theory,

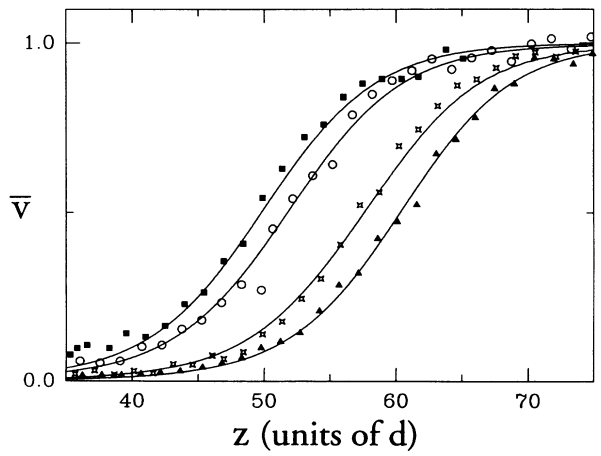

FIG. 26. Normalized velocity profiles from experiment (data points) and CGL simulation (curves) for $R=3.0$ and $\epsilon=0.029$ ($\bar{\epsilon}=0.025$). Left to right: $\nu=0.011$, 0.016, 0.059, 0.105 S, and CGL noise levels $10^8F_A=12.4$, 5.8, 0.43, 0.13.

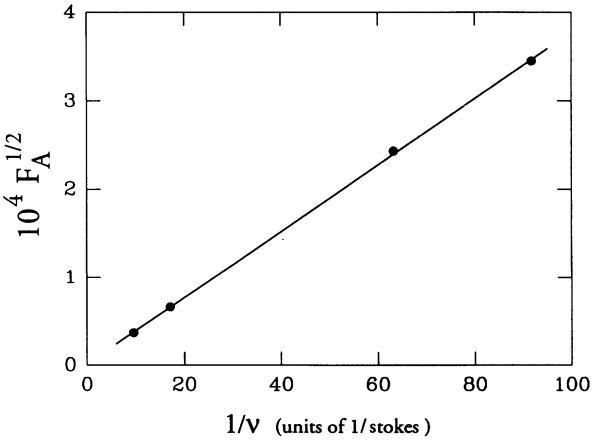

FIG. 27. Experimental noise magnitude vs inverse viscosity.

there would be only a minor shift in the amplitude profiles relative to those observed. For example, for $\tilde{\epsilon}=0.025$ and $R=3.0$, the spatial growth rate is $\beta_m^r=0.20$ and the healing length is $l_h=58$; see Fig. 22. An order of magnitude increase in noise power ($F_A'/F_A=10$) would produce only about a 10% shift in the healing length:

$$\Delta l_h/l_h \approx (1/2\beta_m^r)\ln(F_A'/F_A)l_h = 5.8/58 .$$

IX. CONCLUSIONS

We have presented an extensive, quantitative study of noise amplification *via* convective instability in open Taylor-Couette flow at low axial Reynolds numbers. Theory and experiment agree in nearly every respect, and most phenomena are described quantitatively by a complex Ginzburg-Landau equation. Detailed knowledge of the stability properties and amplification mechanism allowed us to determine properties of the noise source.

The simplicity of the Taylor-Couette geometry allows for precision experimental work and relatively simple and accurate numerical analysis. Except for a short inlet region, the base flow is independent of streamwise position, and the stability properties are global. There are no observed secondary instabilities at low R, and the system is essentially one dimensional, as evidenced by the close agreement between experiment and the one-dimensional CGL equation derived from the Navier-Stokes equations.

Other open flows, typified by jets, wakes, or boundary layers, are more complex and tend to be studied at higher Reynolds numbers. Flow states and stability vary with streamwise position [15], and structure may dissipate as it is carried downstream. Instability is often of a shear nature and typically leads to higher order instabilities in higher dimensions as Reynolds numbers are increased. Work as quantitative as that presented here is difficult or impossible in such cases.

It would be of interest to test the generality of some of the results found here. For example, several "real" open flows, such as object wakes, have regions of both absolute and convective instability which may depend on both external conditions and streamwise position [15]. The appearance of a broadened frequency spectrum and a random phase walk may prove to be a useful diagnostic for locating the transition from absolute to convective instability.

The source of the noise in the open Taylor-Couette experiment, and in particular the fundamental question of whether it may be of thermal origin, is at present not answered. However, the noise is extremely small, and from a practical standpoint it is perhaps more important to have shown in detail how secondary flows can emerge from such small fluctuations. Certainly attempts to reduce free-stream turbulence in (for example) convectively unstable wakes and jets would be limited by some noise source. Because the characteristic growth length of a secondary flow varies only logarithmically with the noise strength, even a drastic reduction in noise would do little to suppress noise-sustained structure in a large-aspect-ratio system, even when the noise is far above the thermal level to begin with.

In sum, this quantitative examination of noise amplification, based on a detailed knowledge of stability properties and amplification mechanism, and comparison with theoretical models based on first principles, may prove useful in extending our understanding of stochastic effects to more complicated flows and to nonequilibrium systems in general.

ACKNOWLEDGMENTS

It is a pleasure to thank Rudy Stuber and Ken Volker for their invaluable help in designing and producing our precise Taylor-Couette columns. We are also grateful to Jack Swift and Pierre Hohenberg for their patience in calculating the noise strength, and for allowing us to use their results prior to publication, and to Manfred Lücke and Arthur Recktenwald for sharing their results. Valuable comments and discussions were contributed by Robert J. Deissler, Hanns Walter Müller, Ingo Rehberg, Steven Trainoff, and Morten Tveitereid. This work was supported by the National Science Foundation under Grant No. DMR91-17428.

[1] J. Leconte, Philos. Mag. **15**, 235 (1858).
[2] E. Berger and R. Wille, Annu. Rev. Fluid Mech. **4**, 313 (1972).
[3] H. A. Becker and T. A. Massaro, J. Fluid Mech. **31**, 435 (1968).
[4] C. E. Polymeropoulos and B. Gebhart, J. Fluid Mech. **30**, 225 (1967).
[5] F. M. White, *Viscous Fluid Flow* (McGraw, New York, 1974).
[6] P. Leehey and P. Shapiro, in *Laminar-Turbulent Transition,* edited by R. Eppler and H. Fasel (Springer, New York, 1979).
[7] M. E. Goldstein, J. Fluid Mech. **154**, 509 (1985).
[8] P. Hall and F. T. Smith, Eur. J. Mech. B **8**, 179 (1989).
[9] See, for instance, D. J. Tritton, *Physical Fluid Dynamics,* 2nd ed. (Oxford University Press, Oxford, 1988).
[10] M. F. Schatz, R. P. Tagg, H. L. Swinney, P. F. Fischer, and A. T. Patera, Phys. Rev. Lett. **66**, 1579 (1991).
[11] L. D. Landau and E. M. Lifshitz, *Fluid Mechanics* (Addison-Wesley, Reading, MA, 1959).
[12] R. J. Deissler, J. Stat. Phys. **40**, 371 (1985); Physica D **25**, 233 (1987).
[13] P. C. Hohenberg and J. B. Swift, Phys. Rev. A **46**, 4773 (1992).
[14] A review of Taylor-Couette flow without through-flow is given by R. C. DiPrima and H. L. Swinney, in *Hydrodynamic Instabilities and Transitions to Turbulence,* edited by H. L. Swinney and J. P. Gollub (Springer, Berlin, 1981).
[15] P. A. Monkewitz, Eur. J. Mech. B **9**, 395 (1990), and references therein.

[16] Convective vs absolute instability in the closed Taylor-Couette system (i.e., without through-flow) has been examined for the case of counterrotating cylinders by R. Tagg, W. S. Edwards, and H. L. Swinney, Phys. Rev. A **42**, 831 (1990).

[17] H. W. Müller, M. Lücke, and M. Kamps, Europhys. Lett. **10**, 451 (1989).

[18] H. W. Müller, M. Lücke, and M. Kamps, Phys. Rev. A **45**, 3714 (1992).

[19] H. W. Müller, M. Lücke, and M. Kamps, in *Ordered and Turbulent Patterns in Taylor-Couette Flow,* Vol. 297 of *NATO Advanced Study Institute, Series B: Physics,* edited by D. Andereck and F. Hayot (Plenum, New York, 1992).

[20] K. L. Babcock, G. Ahlers, and D. S. Cannell, Phys. Rev. Lett. **67**, 3388 (1991).

[21] K. L. Babcock, D. S. Cannell, and G. Ahlers, Physica D **61**, 40 (1992).

[22] A. Tsameret and V. Steinberg, Europhys. Lett. **14**, 331 (1991).

[23] A. Tsameret and V. Steinberg, in *Spontaneous Formation of Space-Time Structures and Criticality,* Vol. 349 of *NATO Advanced Study Institute, Series C: Mathematical and Physical Sciences* edited by T. Riste and D. Sherrington (Kluwer, Dordrecht 1991).

[24] A. Tsameret and V. Steinberg, Phys. Rev. Lett. **67**, 3392 (1991).

[25] A. Tsameret and V. Steinberg, Phys. Rev. E **49**, 1291 (1994).

[26] A. Tsameret, G. Goldner, and V. Steinberg, Phys. Rev. E **49**, 1309 (1994).

[27] J. B. Swift, K. L. Babcock, and P. C. Hohenberg, Physica A **204**, 625 (1994).

[28] R. J. Deissler and H. R. Brand, Phys. Lett. **130**, 293 (1988).

[29] W. Schöpf and I. Rehberg, Europhys. Lett. **17**, 321 (1992).

[30] I. Rehberg, S. Rasenat, M. de la Torre-Juarez, W. Schöpf, F. Hörner, G. Ahlers, and H. R. Brand, Phys. Rev. Lett. **67**, 596 (1991), and unpublished.

[31] E. Bodenschatz, S. Morris, J. de Bruyn, D. S. Cannell, and G. Ahlers, in *Proceedings of the KIT International Workshop on the Physics of Pattern Formation in Complex Dissipative Systems,* edited by S. Kai (World Scientific, Singapore, 1992), p. 227; and M. Wu, G. Ahlers, and D. S. Cannel (unpublished).

[32] M. A. Dominguez-Lerma, D. S. Cannell, and G. Ahlers, Phys. Rev. A **34**, 4956 (1986).

[33] General Magnaplate California, 2701 Palm Dr., Ventura, CA 93003.

[34] Fluoron, Mechanical Seal Division, 4412 Corp. Center Dr., P. O. Box 520, Los Alamitos, CA 90720.

[35] These observations are at odds with the suggestion of Refs. [23] and [24] that sustained structure might be due to reflection from the downstream end.

[36] Kalliroscope Corporation, P. O. Box 60, Groton, MA 01450, rheoscopic liquid AQ-1000. See also P. Matisse and M. Gorman, Phys. Fluids **27**, 759 (1984).

[37] R. Heinrichs, D. S. Cannell, G. Ahlers, and M. Jefferson, Phys. Fluids **31**, 250 (1988).

[38] This value agrees well with interpolation of known values for nearby radius ratios; see Ref. [39].

[39] M. A. Dominguez-Lerma, G. Ahlers, and D. S. Cannell, Phys. Fluids **27**, 856 (1984).

[40] R. Heinrichs, G. Ahlers, and D. S. Cannell, Phys. Rev. Lett. **56**, 1794 (1986).

[41] R. C. DiPrima, J. Fluid Mech. **9**, 621 (1960); R. J. Donnelly and D. Fultz, Proc. Nat. Acad. Sci. U.S.A. **46**, 1150 (1960); H. A. Snyder, Proc. R. Soc. London Ser. A **265**, 198 (1961); S. Chandrasekhar, *ibid.* **265**, 188 (1962).

[42] F. H. Busse, in *Turbulence and Chaotic Phenomena in Fluids,* edited by T. Tatasumi (Elsevier, Amsterdam, 1984), p. 197.

[43] R. M. Lueptow, A. Docter, and K. Min, Phys. Fluids A **4**, 2445 (1992).

[44] A. Tsameret and V. Steinberg, Phys. Rev. E **49**, 4077 (1994).

[45] R. J. Deissler (private communication).

[46] D. I. Takeuchi and D. F. Jankowski, J. Fluid Mech. **102**, 101 (1981); B. S. Ng and E. R. Turner, Proc. R. Soc. London Ser. A **382**, 83 (1982).

[47] An additional disturbance in the base flow was created throughout the apparatus by fluid dragged by the cylinders. However, its long-wavelength nature placed it outside the growing band of wave numbers, and it decayed within a few diffusion times d^2/ν.

[48] This slightly underestimates ϵ_c because we are observing decay of finite amplitude pulses, but the error is negligible at the low axial Reynolds numbers used here.

[49] The cylinder velocity is used to scale velocity, rather than ν/d, to yield better behavior in the narrow-gap limit $\eta \to 1$.

[50] A. Recktenwald, Diplom thesis, Universität des Saarlandes, Saarbrücken, 1992; A. Recktenwald, M. Lücke, and H. W. Müller, Phys. Rev. E **48**, 4444 (1993).

[51] A. C. Newell, Lect. Appl. Math. **15**, 157 (1974).

[52] More recently, the value $c_2 = 0.0113R$ quoted in Ref. [17] was revised [18] to $c_2 = 0.0026R$. The very recent calculations for Taylor-vortex flow by Recktenwald and coworkers [50] yielded $c_2 \simeq 0.0033R$. However, even the unrealistically large value of Ref. [17] had only a very small effect on the results.

[53] G. Dee and J. S. Langer, Phys. Rev. Lett. **50**, 383 (1983).

[54] A. Bers, in *Basic Plasma Physics I,* edited by A. A. Galeev and R. N. Sudan (North-Holland, New York, 1983); R. J. Briggs, *Electron-Stream Interaction With Plasmas* (MIT Press, Cambridge, MA, 1964).

[55] R. Graham, Phys. Rev. A **10**, 1762 (1974).

[56] J. B. Swift and P. C. Hohenberg, Phys. Rev. A **15**, 319 (1977).

[57] See, for instance, Eq. (B.16) of Ref. [27].

[58] W. H. Press, B. P. Flannery, S. A. Teukolsky, and W. T. Vetterling, *Numerical Recipes, the Art of Scientific Computing* (Cambridge University Press, Cambridge, England, 1986).

[59] In earlier simulations for which noise properties were not critical (e.g., in Fig. 11 and Ref. [20]), we added noise at the upstream bounding gridpoint $A[0]$ only.

[60] In doing these calculations it is simpler (but less conceptually clear) to impose constraints on the inverse relation $\omega(\beta)$. For example, $\omega^i = 0$ gives an implicit relation $\beta^r(\beta^i)$, and the extremal constraint $\partial\beta^r/\partial\beta^i = 0$ then gives ω_m; see Ref. [12].

[61] We checked that the anomalous exponent was not an artifact of the demodulation procedure. A discrete analysis, in which locations of time series maxima were compared to those in a periodic pattern having the same mean frequency, gave the same exponents.

[62] J. Feder, in *Spontaneous Formation of Space-Time Structures and Criticality* [23].

[63] For pulses, the initial decay is enhanced by the damping of the frequency and spatial content of the disturbance that lies outside of the resonant band.
[64] One must in principle include temperature fluctuations, but these turn out to be less important than velocity fluctuations, even in cases such as thermal convection in which the temperature is coupled to macroscopic dynamical variables; see Refs. [13,55,56].
[65] C. W. Meyer, G. Ahlers, and D. S. Cannell (unpublished).
[66] V. M. Zaitsev and M. I. Shliomis, Zh. Eksp. Teor. Fiz. **59**, 1583 (1970) [Sov. Phys. JETP **32**, 866 (1971)].
[67] M. Lücke and A. Recktenwald, Europhys. Lett. **22**, 559 (1993).
[68] R. J. Deissler, Phys. Rev. E **49**, R31 (1994).
[69] M. Treiber (unpublished).
[70] The present estimates for thermal noise supersede those of Ref. [21], for which g was set to 1.
[71] Equations (8.4) holds more generally for corotation of the inner and outer cylinders (Ref. [27]). The noise strength at onset is then a function of the angular velocity of the outer cylinder.
[72] These numerical results differ from those quoted by Swift, Babcock, and Hohenberg [27] by a factor $(1-\eta)^2=0.069$ because those authors scaled length by the outer radius $\tilde{r}_2$ rather than by the gap $d=\tilde{r}_2-\tilde{r}_1$.
[73] In Ref. [32] it had been found that the weakest flow detectable visually with Kalliroscope corresponds to an amplitude A of about 0.10 using our value of g (0.003 with $g=1$). This value depends somewhat on experimental conditions such as geometry, Kalliroscope concentration, fluid viscosity, and illumination. It is not surprising that the present method gives somewhat smaller minimum detectable amplitudes.
[74] We do not display data for which $\tilde{\epsilon}_s<0.01$ because for those the uncertainty in F_A is excessively large due to uncertainty in $\tilde{\epsilon}_s$.
[75] V. Steinberg (private communication).

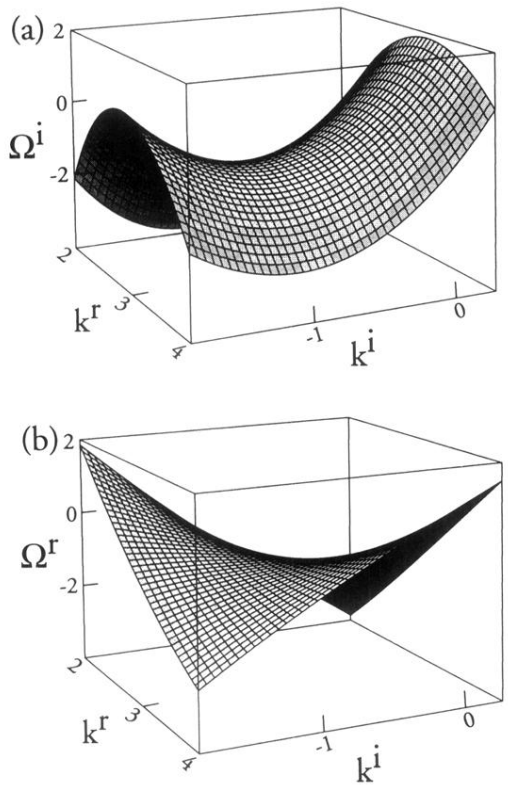

FIG. 8. Imaginary and real parts of the complex dispersion relation $\Omega(k)$ in the Navier-Stokes equations for convectively unstable conditions $\epsilon=0.036$ and $R=3.0$. (a) Growth rate Ω^i. (b) Angular frequency Ω^r.